Design of a Magnetorheological Brake System Based on Magnetic Circuit Optimization

by

Kerem Karakoc
BSc - Bogazici University, TURKEY, 2005

A Thesis Submitted in Partial Fulfillment of the
Requirements for the Degree of
Master of Applied Science
in the
Department of Mechanical Engineering.

University of Victoria

Supervisory Committee

Dr. Edward Park, Supervisor (Dept. of Mechanical Engineering,
University of Victoria)

Dr. Afzal Suleman, Supervisor (Dept. of Mechanical Engineering,
University of Victoria)

Dr. Zuomin Dong, Member (Dept. of Mechanical Engineering,
University of Victoria)

Dr. Farid Golnaraghi, External Examiner (School of Engineering Science,
Simon Fraser University)

Supervisors: Dr. Edward Park and Dr. Afzal Suleman

Abstract

Conventional hydraulic brake (CHB) systems used in automotive industry have several limitations and disadvantages such as the response delay, wear of braking pad, requirement for auxiliary components (e.g. hydraulic pump, transfer pipes and brake fluid reservoir) and increased overall weight due to the auxiliary components. In this thesis, the development of a novel electromechanical brake (EMB) for automotive applications is presented. Such brake employs mechanical components as well as electrical components, resulting in more reliable and faster braking actuation. The proposed electromagnetic brake is a magnetorheological (MR) brake.

The MR brake consists of multiple rotating disks immersed into an MR fluid and an enclosed electromagnet. When current is applied to the electromagnet coil, the MR fluid solidifies as its yield stress varies as a function of the magnetic field applied by the electromagnet. This controllable yield stress produces shear friction on the rotating disks, generating the braking torque. This type of braking system has the following advantages: faster response, easy implementation of a new controller or existing controllers (e.g. ABS, VSC, EPB, etc.), less maintenance requirements since there is no material wear and lighter overall weight since it does not require the auxiliary components used in CHBs.

The MRB design process included several critical design steps such as the magnetic circuit design and material selection as well as other practical considerations such as cooling and sealing. A basic MRB configuration was selected among possible candidates and a detailed design was obtained according to a set of design criteria. Then, with the help of a finite element model (FEM) of the MRB design, the magnetic field intensity distribution within the brake was simulated and the results were used to calculate the braking torque generation.

In order to obtain an optimal MRB design with higher braking torque generation capacity and lower weight, the key design parameters were optimized. The optimization procedure also consisted of the FEM, which was required to calculate the braking torque generation in each iteration. Two different optimization search methods were used in obtaining the minimum weight and maximum braking torque: (i) a random search algorithm, simulated annealing, was first used to find an approximate optimum design and (ii) a gradient based algorithm, sequential quadratic programming, was subsequently used to obtain the optimum dimensional design parameters.

Next, the optimum MRB was prototyped. The braking performance of the prototype was tested and verified, and the experimental results were shown. Also, experimental results were compared with the simulation results. Due to the lack of accurate material property data used in the simulations, there were discrepancies between the experimental and the simulation results.

Other possible sources of errors are also discussed. Since the prototype MRB generates much lower braking torque compared to that of a similar size CHB, possible design improvements are suggested ton further increase the braking torque capacity. These include the relaxation of the optimization constraints, introduction of additional disks, and the change in the basic magnetic circuit configuration.

Dr. Edward Park, Supervisor (Dept. of Mechanical Engineering,
University of Victoria)

Dr. Afzal Suleman, Supervisor (Dept. of Mechanical Engineering,
University of Victoria)

Dr. Zuomin Dong, Member (Dept. of Mechanical Engineering,
University of Victoria)

Dr. Farid Golnaraghi, External Examiner (School of Engineering Science,
Simon Fraser University)

Contents

List of Figures

List of Tables

Nomenclature

A	Cross-sectional area of medium $[m^2]$
A_{ws}	Working surface area $[m^2]$
d_{brake}	Outer diameter of MRB $[m]$
f_0	Speed effect coefficient
f_s	Basic coefficient
F_f	Friction force $[N]$
F_L	Transfer of weight caused by braking $[N]$
F_n	Normal force $[N]$
F_r	Rolling resistance force $[N]$
g	Gravitational acceleration $[ms^{-2}]$
h	MR fluid gap thickness $[m]$
h_cg	Height of the center of gravity $[m]$
H_{core}	Magnetic field intensity on magnet core $[A/m]$
H_{disk}	Magnetic field intensity on disk section $[A/m]$
H_{gap}	Magnetic field intensity on electromagnet gap that includes H_{disk} and H_{MRF} $[A/m]$
H_{MRF}	Magnetic field intensity on MRF $[A/m]$
i	Current applied to the coil $[A]$
I	Total moment of inertia $[kgm^2]$
I_e	Engine inertia $[kgm^2]$
I_w	Wheel's inertia $[kgm^2]$
I_y	Inertia of brake disks $[kgm^2]$
k	Linear coefficient relates intensity to yield stressgenerated on MRF
k_{con}	Thermal conductivity $[W/m-K]$
k_T	Weighting coefficient for torque
k_W	Weighting coefficient for weight
K_v	Conversion factor (m/s to mph) $[mph(m/s)^{-1}]$
l	Length of medium $[m]$

l_{base}	Wheel base $[m]$
l_{core}	Length of magnet core $[m]$
l_{disk}	Length of total disk section $[m]$
l_{gap}	Length of electromagnet gap that includes l_{disk} and l_{MRF} $[m]$
l_{MRF}	Length of total MRF section $[m]$
m_t	Quarter vehicle mass $[kg]$
m_v	Vehicle mass $[Kg]$
m_w	Wheel mass $[Kg]$
n	Number of wire turns in coil
N	Number of disks
Q	Heat transferred $[Cal]$
r	Radius of shear disk $[m]$
$r_z \& r_j$	Outer and inner radii of the shear disk $[m]$
R_w	Wheel Radius $[m]$
s_r	Slip ratio
S	Heat transfer surface $[m^2]$
T	Magnetic torque generated in MRB, i.e. T_H $[Nm]$
∇T	Temperature gradient $[K/m]$
T_μ	Viscous torque $[Nm]$
T_b	Braking torque $[Nm]$
T_H	Torque generated due to applied field $[Nm]$
T_{ref}	Reference torque value $[Nm]$
u	Linear fluid velocity $[m/s]$
w	Angular velocity $[rad/s]$
W	Weight of MRB $[N]$
W_{ref}	Reference weight value $[N]$
x	Horizontal distance travelled $[m]$
$\dot{x}$	Linear velocity, $[m/s]$
$\ddot{x}$	Linear acceleration $[m/s^2]$
y	Vertical distance $[m]$
$\mathbf{d}$	Dimensional design parameters vector
$\mathbf{B}$	Magnetic flux density vector $[T]$
$\mathbf{D}$	Electric displacement $[C/m^2]$
$\mathbf{E}$	Electric field intensity $[N/C]$
$\mathbf{J}$	Current density vector $[A/m^2]$
$\mathbf{H}$	Magnetic field intensity vector $[A/m]$

Greek Symbols

$\ddot{\theta}$	Angular acceleration $[rad/s^2]$
θ	Angular Distance $[rad]$
ρ	Electric charge density $[C/m^3]$
μ_f	Friction coefficient
φ	Gear ration
μ	Magnetic permeability $[H/m]$
$\Re$	Magnetic reluctance $[turns/H]$
μ_p	Plastic viscosity $[kg/m.s]$
β	Power coefficient that relates intensity to yield stressgenerated on MRF
μ_r	Relative magnetic permeability
$\dot{\gamma}$	Shear rate $[Hz]$
τ	Total shear stress $[Pa]$
μ_0	Vacuum permeability $[H/m]$
τ_H	Yield stress of MRF due to applied field $[Pa]$

Acronynms

ABS	Anti-lock Brake System
AISI	American Iron and Steel Institute
AWG	American Wire Gauge
CAD	Computer Aided Design
CHB	Conventional Hydraulic Brake
EMB	Electro-Mechanical Brake
EPB	Electronic Parking Brake
FEA	Finite Element Analysis
FEM	Finite Element Model
LB	Lower Boundary
mmf	Magnetomotive Force
MR	Magnetorheological
MRB	Magnetorheological Brake
MRF	Magnetorheological Fluid
PID	Proportional-Integral-Derivative
SA	Simulated Annealing
SQP	Sequential Quadratic Programming
UB	Upper Boundary
VSC	Vehicle Stability Control

Acknowledgements

I would like to thank Dr. Edward Park and Dr. Afzal Suleman for giving me the opportunity to be a part of their research team. Also, I would like to thank them for sharing their academic expertise and life experience with me.

Special appreciation to Patrick Chang for the help in setting up the experiment. His effort, availability, patience and know-how were very valuable. Special thanks to Rodney Katz and Ken Begley for the help with the machining of the parts and for helping me to gain valuable experiences in terms of manufacturing processes and drawings.

I also thank Casey Keulen for his help in understanding the existing experimental setup at the beginning of my program. I give thanks to Luis Falco da Luz for his previous work with the experimental setup and Dilian Stoikov for his previous work related to control.

I would also like to thank Sandra Makosinski for all the help and sincerity. Thanks for always being there when I needed help. Also, I would like to express my appreciation to Art Makosinski for his logistic support and for sharing his immense practical knowledge.

Special thanks to Kelly Sakaki and Dan Kerley. They made me feel like a Canadian and made the lab a pleasant place to work. I also thank to Jung Keun Lee, William Liu, Vishalini Bundhoo, Ricardo Paiva, Andre Carvalho, Casey Keulen, Adel Younis and others for their friendship.

I would like to express my gratitude to Dr. Mehmet Yildiz, for his infinite support, help and encouragement.

I thank Kerem Gurses for accompanying me in this journey. It has been my pleasure to share the same apartment and the same name.

I also thank Dr. Emre Karakoc, my brother, for his support and directions. He

was the one who offered me to apply for a Master's position at UVic. I thank him for helping me to set my future goals by sharing his experience in life with me.

A final word of gratitude has to go to my parents for their continuous support and faith in me. I know there is no way to repay my debt, but all I can do is to make them proud. Without their support and love, I would not be able to succeed.

To my family...

Chapter 1

Introduction

Automotive industry is changing everyday. Billions of dollars are invested in research and development for building safer, cheaper and better performing vehicles. One such investment is the "x by wire"topic which has been introduced to improve the existing mechanical systems on automobiles. This term means that the mechanical systems in the vehicles can be replaced by electromechanical systems that are able to do the same task in a faster, more reliable and accurate way than the pure mechanical systems.

This thesis work is concerned with the topic of braking in the vehicles. Nowadays, conventional hydraulic brakes (CHB) are being used in order to provide the required braking torque to stop a vehicle. This system involves the brake pedal, hydraulic fluid, transfer pipes and brake actuators (disk and drum brakes). When the driver presses on the brake pedal, the hydraulic brake fluid provides the pressure in the brake actuators that squeezes the brake pads onto the rotor. The basic block diagram of this type of brake is shown in Figure 1.1 (right).

However, the CHB has a number of disadvantages. First of all, when the driver

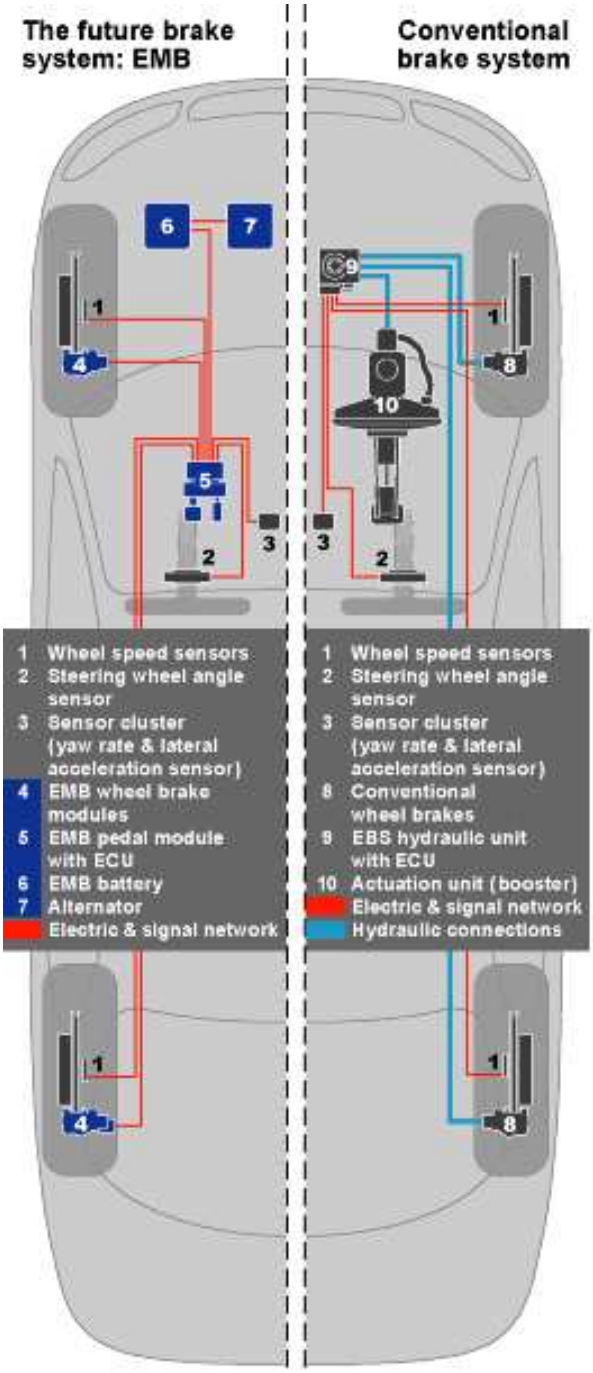

Figure 1.1: Comparison of a CHB system and an electromechanical brake (EMB) system on a passenger type car [1]

pushes the pedal, there is a latency in building up the pressure necessary to actuate the brakes. Also, since CHBs employ a highly pressurized brake fluid, there is the possibility of leakage of the brake fluid that would cause fatal accidents, and this fluid is harmful to the environment as well.

Another problem seen in CHBs is that this type of brake uses the friction between brake pads and the brake disk as its braking mechanism, leading to the brake pad wear. Due to both the material wear and the friction coefficient variation in high speeds, the brake performs less optimally in high speed region, as well as with the increased number of usage cycles. Thus, the brake pads must be changed periodically in order to get the optimum braking performance. Finally, another disadvantage of this type of brake system is that it is bulky in size, when both auxiliary components and brake actuators are considered.

Nowadays in addition to the use of the CHB, pneumatically actuated drum brakes (i.e. air brakes) are being used for trucks and other heavy vehicles that need more braking torque. Similar to the CHB, in this type of brake, pneumatic pumps and pipes are used to transfer the air pressure to the brake actuators.

However, with the introduction of "x by wire" technologies, electromechanical brakes (EMB) have appeared in the industry. In this configuration, some of the pure mechanical components of the conventional brakes are replaced by electromechanical components. Figure 1.1 (left) shows a typical EMB system. A simple example of such brake system is the drum brakes used in trailers where less braking torque is required. These brakes are actuated by an electromagnet installed in the drum brake instead of a hydraulic mechanism that attracts a magnetic rotating disks onto a stator. The friction generated between the stator and the rotor results in braking. Electric calipers developed by Continental [1] and Delphi [2] are also examples where the hydraulic actuators are replaced with electromechanical ones. There are also eddy

current retarders being used for trucks, buses, trains and garbage collectors. This type of brake basically works in conjunction with the main hydraulic brakes, in order to decrease the braking load [3]. Eddy current brakes [4, 5, 6, 7] cannot be used alone due to their performance loss (i.e. low braking torque generation) in the low speed region.

In Table 1.1, the disadvantages of a CHB and the potential advantages of an EMB are listed.

Table 1.1: Disadvantages of a CHB and the potential advantages of an EMB

Disadvantages of CHB	**The Potential Advantages of EMB**
- Slow response due to pressure build-up	- Faster response
- Control that requires additional electrical components	- Easy implementation of control systems
- Significant Weight of the overall system	- Reduced number of components and wiring
- Brake pad wear	- Less maintenance due to elimination of pads
- Risk of environmentally hazardous brake fluid leakage	- Elimination of hazardous brake fluid
	- Simple software-based brake parameter adjustment depending on the driving conditions

In this thesis work, an EMB based on magnetorheological fluids (MR fluid or MRF), i.e. a magnetorheological brake (MRB), is presented. MRB is a friction based brake like a CHB. However, the method of the friction generation in an MRB is entirely different. In the CHB, when the braking pressure is applied, the stator and rotor surfaces come together and friction is generated between the two surfaces, resulting in the generation of the braking torque. But in the MRB, MRF is filled between the stator and the rotor, and due to controllable rheological characteristics

of the MRF, shear friction is generated (thus the braking torque).

MR fluids are created by adding micron-sized iron particles to an appropriate carrier fluid such as oil, water or silicon. Their rheological behavior is almost the same as that of the carrier when no external magnetic field is present. However, when exposed to a magnetic field, the iron particles acquire a dipole moment aligned with the applied magnetic field to form linear chains parallel to the field [8, 9]. This reversibly changes the liquid to solid-like that has a controllable yield strength, which its magnitude depends directly on the magnitude of the applied magnetic field. There is a number of companies producing MR fluids, e.g. Lord Corporation, for various applications such as clutches, dampers, brakes, as well as for medical and seismic applications.

Although the studies on MRFs started around the late 1800s and early 1900s, the first relevant patent was issued to Jacob Rabinow [10, 11] in 1940s [12]. The interest in MR technology rose in the late 1980s and since then, a number of commercial and research devices have appeared: e.g. hydraulic systems [13], damping systems and seismic devices [14, 15, 16, 17, 18], clutches [10, 19, 20], prosthetic devices [21, 22], haptic devices [23], cancer treatment equipments [24] and exercise equipments [25, 26]. Also, a study on possible applications of MRF devices was done by Carlson *et al.* in [27].

The main contribution of this thesis work is the development of a new MRB configuration for automotive application. The MRB is a pure electronically controlled actuator and as a result, it has the potential to further reduce the braking time (thus, braking distance), as well as easier integration of existing and new advanced control features such as anti-lock braking system (ABS), vehicle stability control (VSC), electronic parking brake (EPB), etc. (see Table 1.1).

The idea of using the friction generated by aligned magnetic materials under

magnetic field in brakes was first introduced by Eddens [28, 29, 30]. He devised a brake which contains small magnetic particle powder and when magnetic field is applied, the powder aligns in the direction of applied magnetic field and generates a resistance against motion. With the subsequent introduction of MRFs, the dry magnetic particle powder has been replaced by these fluids as the source of friction for braking purposes. The literature presents a number of MRF based brake designs, e.g. [31, 32, 33, 34, 35], and modeling, design, optimization and control issues of MRBs were also considered in a few previous works [34, 36, 37, 38].

The basic configuration of a MRB proposed by Park *et al.* [34] for the automotive application is shown in Figure 1.2. In this configuration, a rotating disk (3) is enclosed by a static casing (5), and the gap (7) between the disk and casing is filled with the MR fluid. A coil winding (6) is embedded on the perimeter of the casing and when electrical current is applied on the coil, due to the generated magnetic fields, the MR fluid in the gap becomes solid-like instantaneously. The shear friction between the rotating disk and the solidified MR fluid provides the required braking torque. Unlike previous works, in this work, a new MRB is designed with a focus on magnetic circuit design and material selection.

1.1 Thesis Objective

The main objective of this thesis is to develop an MRB specifically for automotive application, with the potential advantages listed in Table 1.1. Within this main objective, the thesis has the following sub-objectives:

1. Creating an accurate electromagnetic finite element model (FEM) of the MRB that simulates the braking behavior;

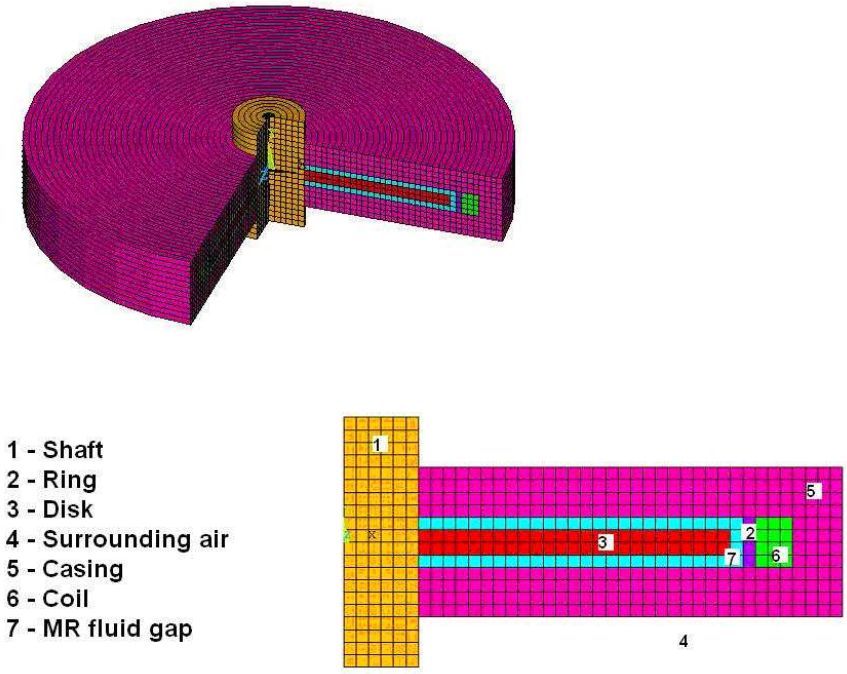

Figure 1.2: Cross section of an MRB actuator design [34, 38]

2. Selection of proper materials for the MRB with adequate structural, thermal and magnetic properties;

3. Detailed design of the MRB with considerations to sealing and cooling as well as applied current density, viscous torque generation and the number of shear disks;

4. Optimization of the magnetic circuit in the MRB for higher braking torque capacity; and

5. Validation of the finite element simulations with an experimental prototype.

1.2 Thesis Outline

In Chapter 2, the dynamic model of a typical passenger vehicle is introduced and the braking torque requirements are calculated for different vehicles (i.e. a fully loaded car, a sport motorbike and a scooter). After the required braking torque values are obtained, the analytical model of an MRB is presented. The behavior of MR fluid is modeled using the Bingham plastic model. Then, by using this model, the total braking torque generated is analytically described in terms of the magnetic field intensity applied and the viscosity of the fluid.

In Chapter 3, the design process of an MRB is explained in detail. The proposed MRB is designed considering the design criteria such as the number of disks used, the dimensional design parameters, the materials used and the configuration of the magnetic circuit. There are also some additional practical considerations that are included during the design process, e.g. sealing of the MR fluid, cooling the MRB and the viscous torque generated within the MRB due to MR fluid viscosity. However, the main focus of the design process is on magnetic circuit design and material selection.

In this chapter, corresponding dimensional design parameters are introduced and the MRB that is designed in detail according to the above design criteria is presented.

In Chapter 4, in order to calculate the total braking torque generation, a FEM of the MRB is created solving the magnetic field intensity distribution within the brake. A commercial FEA software package, Comsol Multiphysics®, is used for this purpose. Then, the MRB is optimized for higher braking torque and lower overall weight using the FEM created. An optimization problem is defined and proper search methods are selected to solve for optimal torque and weight. At the end of this chapter, an optimum MRB design is found and presented, with the optimum dimensional design parameter. Then, the magnetic field intensity, the magnetic flux density and the shear stress distribution plots of the optimum design are shown. Finally, using the FEM, the braking torque generation is simulated at various current values applied to the coil.

Chapter 5 presents the experimental results. A CAD model of the optimized MRB is generated using a 3-D CAD software, Pro/E. In order to verify the simulation results obtained in the previous chapter, a prototype made based on the CAD model. Then, the prototype is mounted on an experimental test-bed, which consists of a torque source (i.e. servo motor) and a torque sensor. Braking torque generation at various applied currents is recorded and a comparison between the simulation results and the experimental results is made. At the end of this chapter, some concluding remarks are presented comparing the results obtained and the original design requirements.

The conclusions of this work are presented in Chapter 6. In addition, possible improvements that can be made in order to design a higher torque MRB are discussed here as part of future works.

Chapter 2

Modeling of MR Brake

As mentioned in the previous chapter, a magnetorheological brake (MRB) is proposed in this work as a possible substitute for CHBs. In this chapter, before modeling the MRB, the vehicle dynamics are studied in order to calculate the required amount of braking torque for stopping a vehicle. Then, required braking torque values of different vehicles are calculated using the dynamic vehicle model. Finally, an analytical model of the MRB itself, required to obtain the braking torque generation, is derived.

2.1 Vehicle Dynamics

In this work, the motion of a vehicle is described using the quarter vehicle model [39]. This model is needed to calculate the required braking torque that a brake should provide. The basic assumption of this model is that the mass of the vehicle is divided equally between four wheels. In Figure 2.1, a free body diagram of a wheel rotating clockwise is shown. During braking, a torque is applied by the brake, T_b , and F_r, F_f, F_n and F_L are the rolling resistance force, the friction force, normal force and the

transfer of weight caused by braking of the vehicle. Let's denote I as the total mass moment of inertia and $\ddot{\theta}$ is the angular acceleration of the vehicle. The radius of the wheel is R_w and x is the distance traveled by the vehicle.

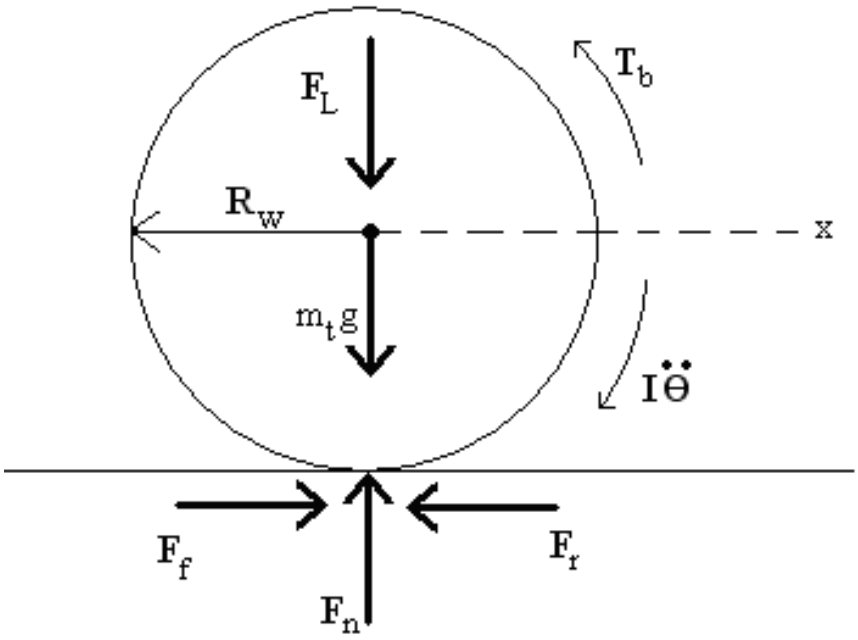

Figure 2.1: Free body diagram of a wheel

According to the quarter vehicle model, the mass that the wheel carries can be calculated as:

$$m_t = \frac{1}{4}m_v + m_w \tag{2.1}$$

where m_v is the mass of the vehicle and m_w is the mass of the wheel. The total mass moment of inertia can be defined defined by:

$$I = I_w + \frac{1}{2}\varphi^2 I_e + I_y \tag{2.2}$$

where I_w is the wheel's inertia, I_e is the engine inertia, φ is the gear ratio and I_y is the inertia of the brake disks. The effective inertia of the engine, $\varphi^2 I_e$, is divided by 2 in order to account for the distribution of the inertia of the engine to each of the driving wheels.

The rolling resistance force against the motion of the wheel is defined as [39]:

$$F_r = f_0 + 3.24 f_s (K_v \dot{x})^{2.5} \tag{2.3}$$

where K_v is a conversion factor that is used for converting the speed value from m/s to mph, f_s and f_0 are the basic coefficient and the speed effect coefficient. This equation was developed by the Institute of Tech. in Stuttgart for rolling on a concrete surface [40].

The friction force acting on the wheel is defined in terms of the normal force and the friction coefficient between the tire and the surface, i.e.

$$F_f = \mu_f F_n \tag{2.4}$$

$$F_n = m_t g - \frac{m_v h_{cg}}{l_{base}} \ddot{x} = m_t g - F_L \tag{2.5}$$

where l_{base} is the wheel base and h_{cg} is the height of the center of gravity and the friction coefficient, μ_f, is a function of the slip ratio, s_r, which is the relative proportion of the rolling to slipping, i.e.

$$s_r = \frac{\dot{x} - R_w w}{\dot{x}} \tag{2.6}$$

where w is the angular velocity of the wheel. The correlation between the slip ratio and the coefficient of friction is illustrated in Figure 2.2 for different types of surfaces.

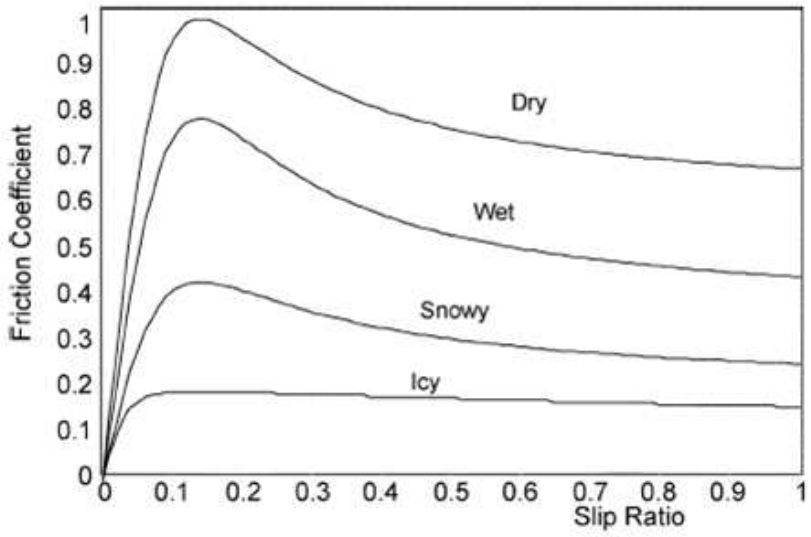

Figure 2.2: Friction coefficient versus slip ratio for different road surfaces [41]

Finally, the equations of motion for the wheel can be written as:

$$m_t\ddot{x} = -F_f = -\mu_f m_t g + \mu_f \frac{m_v h_{cg}}{l_{base}}\ddot{x} \tag{2.7}$$

$$I\ddot{\theta} = -T_b + R_w F_f - R_w F_r = -T_b + \mu_f R_w F_n - R_w F_r \tag{2.8}$$

Eq (2.7) is the force equilibrium equation in the direction of motion and Eq. (2.8) is the moment equilibrium equation around the wheel axis. Then, the required braking torque, T_b, can be found by solving these two equations.

2.1.1 Required Braking Torque Calculation

In this section, required braking torque values for various vehicles were calculated using the above dynamic model of the vehicle. However, in order to solve for the braking torque, the parameters in the equations have to be known. These parameters were taken from Will *et al.* [42] and are listed in Table 2.1.

Table 2.1: Parameters for the quarter car model

Wheel Radius	R_w	0.326 m
Wheel Base	l_{base}	2.5 m
Center of Gravity Height	h_{cg}	0.5 m
Wheel Mass	m_w	40 kg
1/4 of the Vehicle Mass	$m_v/4$	415 kg
Total Moment of Inertia of Wheel and Engine	I_t	1.75 kg.m^2
Basic Coefficient	f_o	10e-2
Speed Effect Coefficient	f_s	0.005
Scaling Constant	K_v	2.237

Approximate required braking torque values for a sport motorbike and a scooter were also calculated. Due to the lack of information on some property values (i.e. f_0,

f_s and K_v), the braking torque requirement for these vehicles were calculated assuming that the whole kinetic energy of the vehicle is dissipated in the brake actuators. With such an assumption, the effects of rolling friction and the friction between the tire and the road were omitted. In Table 2.2, the data used for the required braking torque calculations are summarized.

Table 2.2: Required braking torque values for different vehicles

Properties	Passenger Vehicle	Sport Motorbike	Scooter
Mass (Total-loaded) (kg)	1820 ($m_w = 40$)	370	250
Wheel Size (inch)	13	17	12
Wheel Radius (m)	0.3226	0.305	0.237
Number of Brake Actuators	4	2	2
Assumptions:			
Road Surface	Dry, smooth concrete		
Initial Speed	60 mph (26.82 m/s)		
Deceleration (m/s^2)	5.8 m/s^2		
Braking Torque (Nm)	560	321	171

The above study was carried out in order to determine the braking torque that a comparable MRB should generate. Table 2.2 gives us an idea about how much braking torque must be generated by an MRB.

2.2 Analytical Model of MR Brake

In order to model an MRB, the behavior of the MR fluid under magnetic field application has to be modeled. The idealized characteristics of the MR fluid can be described effectively by using the Bingham-Plastic Model [8, 36, 43, 44, 45]. According to this

model, the total shear stress τ is:

$$\tau = \tau_H \text{sgn}(\dot{\gamma}) + \mu_p \dot{\gamma} \tag{2.9}$$

where τ_H is the yield stress due to applied magnetic field intensity, μ_p is the no-field plastic viscosity of the fluid and $\dot{\gamma}$ is the shear rate. The first term in the right side of the equation is a "magnetic term" related to the applied magnetic field intensity whereas the second term is a "viscous term" related to the viscosity of the MR fluids. The use of the *sgn* function guarantees that the magnetic term will always be added to the viscous term no matter what the direction of the shear rate is. Then, using Eq. (2.9), the braking torque can be defined as follows for the geometry shown in Figure 1.2:

$$T_b = \int_{A_{ws}} \tau r dA_{ws} = 2\pi N \int_j^z (\tau_H \text{sgn}(\dot{\gamma}) + \mu_p \dot{\gamma}) \tag{2.10}$$

where A_{ws} is the working surface area (the domain where the fluid is activated by applied magnetic field intensity), z and j are the outer and inner radii of the disk, N is the number of disks used in the enclosure and r is the radius of the disk.

If the MR fluid gap in Figure 1.2 is very small (i.e. gap thickness << radius of the disk), the shear rate can be obtained by:

$$\dot{\gamma} = \frac{rw}{h} \tag{2.11}$$

which assumes linear fluid velocity distribution across the gap and no slip conditions. In Eq. (2.11), w is the angular velocity of the disk and h is the thickness of the MR fluid gap.

In Eqs. (2.9) and (2.10), the yield stress, τ_H, can be approximated in terms of the magnetic field intensity applied specifically onto the MR fluid, H_{MRF}, and the

constant parameters, k and β, i.e.

$$\tau_H = kH_{MRF}^{\beta} \tag{2.12}$$

where the parameters can be calculated using the shear stress versus applied magnetic field intensity plot published in the specs of the MR fluid. The MR fluid selection and detailed information about the selected MR fluid will be discussed in Sec. 3.10.

By substituting Eqs. (2.11) and (2.12), the braking torque equation in Eq. (2.10) can be rewritten as:

$$T_b = 2\pi N \int_j^z (kH_{MRF}^{\beta}\text{sgn}(\dot{\gamma}) + \mu_p \frac{rw}{h})r^2 dr \tag{2.13}$$

Then, Eq. (2.13) can be divided into the following two parts:

$$T_H = 2\pi N \int_j^z (kH_{MRF}^{\beta}\text{sgn}(\dot{\gamma}))r^2 dr \tag{2.14}$$

$$T_\mu = \frac{\pi}{2h} N\mu_p w(r_z^4 - r_j^4) \tag{2.15}$$

where T_H is the torque generated due to the applied magnetic field and T_μ is the torque generated due to the viscosity of the fluid. Since the magnetic field intensity distribution within the MRB is a function of the radius, the results of the integrations cannot be simplified. Then, finally, the total braking torque is $T_b = T_\mu + T_H$. From the design point of view, the parameters that can be varied to increase the braking torque generation capacity are: the number of disks (i.e. N), the dimensions and configuration of the magnetic circuit (i.e. r_z, r_j, and other dimensional design parameters shown in Figure 3.2), and H_{MRF}, which is related to the applied current density in the electromagnet and materials used in the magnetic circuit.

Chapter 3

Design of MR Brake

In this chapter, the proposed MRB is designed considering the design parameters addressed at the end of the previous chapter (see Sec. 2.2). There are also some additional practical considerations that are included during the design process, e.g. sealing of the MR fluid, cooling the MRB and the viscous torque generated within the MRB due to MR fluid viscosity. Below, the main design criteria considered for the brake are listed, which will be discussed in detail in the subsequent subsections:

1. Magnetic Circuit Design
2. Material Selection
3. Sealing
4. Cooling
5. Working Surface Area
6. Viscous Torque Generation

7. Applied Current Density

8. Additional Disks attached to the shaft

9. MR Fluid Selection

Amongst the various design criteria, the main focus of our design process is on the magnetic circuit design and material selection. Note that Figure 3.1 shows the cross section of the basic MRB configuration which is improved according to the listed design criteria. This is the configuration that will be considered for finite element analysis and design optimization in the subsequent chapter. The corresponding dimensional design parameters are shown in Figure 3.2.

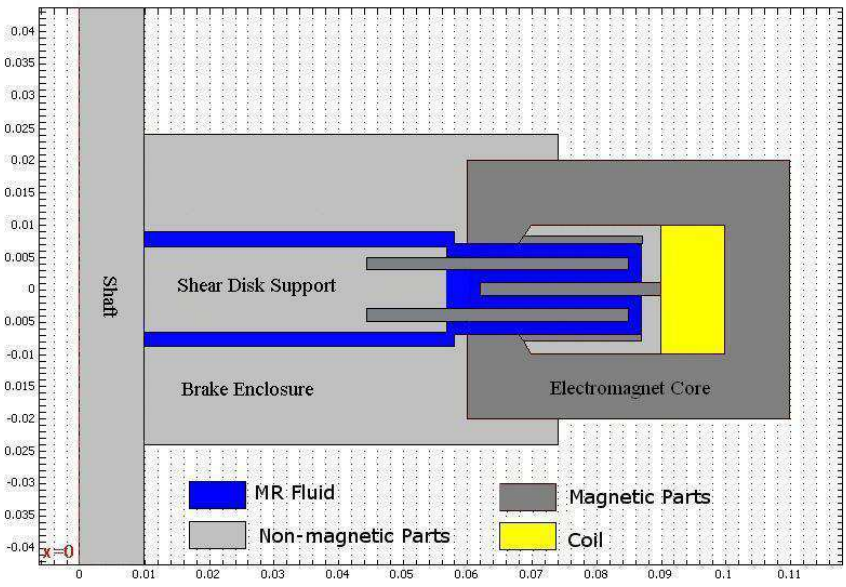

Figure 3.1: Chosen MRB configuration based on the design criteria

Before explaining the above design criteria in detail, a brief discussion on the conceptual design selection procedure, which led to the selection of the basic configuration

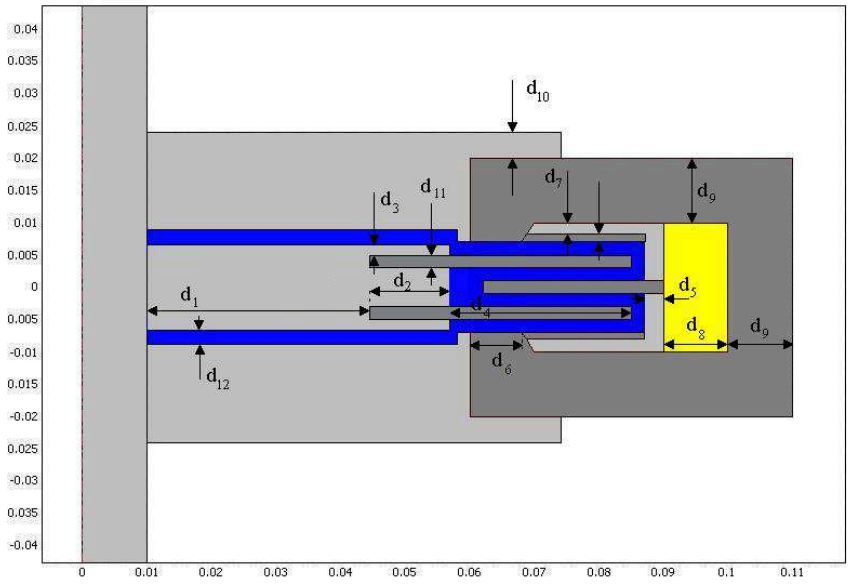

Figure 3.2: Dimensional parameters related to magnetic circuit design

presented in Figure 3.1, is given in Sec. 3.1.

3.1 Conceptual Design Selection

The selected basic configuration of the proposed MRB is presented in Figure 3.1. This selection was made amongst the four candidate conceptual designs shown in Figure 3.3. In this figure, the first design (a) is the selected design with the electromagnet coil embedded into the stator. The second one (b) is slightly different from the first one in terms of the coil cross-sectional area. Unlike (a), the magnetic field intensity generation is increased by increasing the area occupied by the coil is installed. However, this design does not have a magnetic flux focus region and the intensity is generated mostly due to coil field. The third one (c) is a totally different design from the others with the coil installed on the rotating shear disk. Last one (d) is another design with a different magnetic circuit configuration and magnetic focus region. Unlike the others, this design has two separate coil regions, where the coils are wound around the C-shaped magnetic part used to focus the magnetic flux on both sides.

Based on our initial analysis (using FEA), the design (c) is the one that can generate the most braking torque. However, since the coil is installed on the rotating shear disk, it can not be easily manufactured. Therefore, the first design, (a), whose cross-section was shown in Figure 3.1, was selected mainly due to manufacturability.

3.2 Magnetic Circuit Design

The main goal of the magnetic circuit analysis performed in this work is to direct the maximum amount of the magnetic flux generated by the electromagnet onto the MR

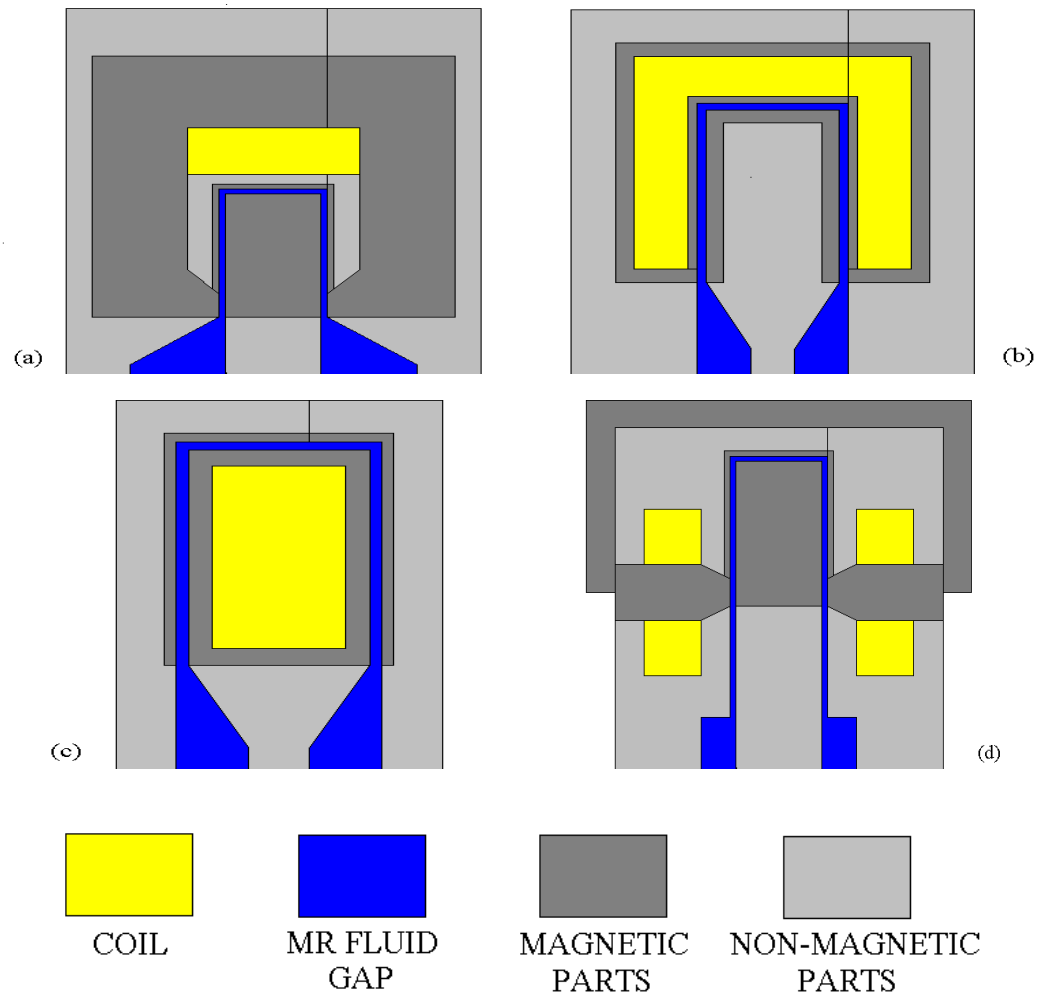

Figure 3.3: Four candidate designs

fluid located in the gap. This will allow the maximum braking torque to be generated.

As shown in Figure 3.4, the magnetic circuit in the MRB consists of the coil winding in the electromagnet, which is the magnetic flux generating "source" (i.e. by generating magnetomotive force or *mmf*), and the flux carrying path. The path provides resistance over the flux flow, and such resistance is called reluctance ($\Re$). Thus, in Figure 3.4, the total reluctance of the magnetic circuit is the sum of the reluctances of the core and the gap, which consists of the MR fluid and the shear disk (see Figure 3.1). Then, the flux generated (ϕ) in a member of the magnetic circuit in Figure 3.4 can be defined as:

$$\phi = \frac{ni}{\Re} = \frac{mmf}{\Re} \tag{3.1}$$

where:

$$\Re = \frac{l}{\mu A} \tag{3.2}$$

In Eq. (3.1), n is the number of turns in the coil winding and i is the current applied; in Eq. (3.2), μ is the permeability of the member, A is its cross-sectional area, and l is its length. Recall that in order to increase the braking torque, the flux flow over the MR fluid needs to be maximized. This implies that the reluctance of each member in the flux path of the flux flow has to be minimized according to Eq. (3.1), which in turn implies that l can be decreased or/and μ and A can be increased according to Eq. (3.2).

However, since the magnetic flux in the gap (ϕ_{gap}) and in the core (ϕ_{core}) are different, the magnetic fluxes cannot be directly calculated as the ratio between the *mmf* and the total reluctance of the magnetic circuit. Note that magnetic flux can

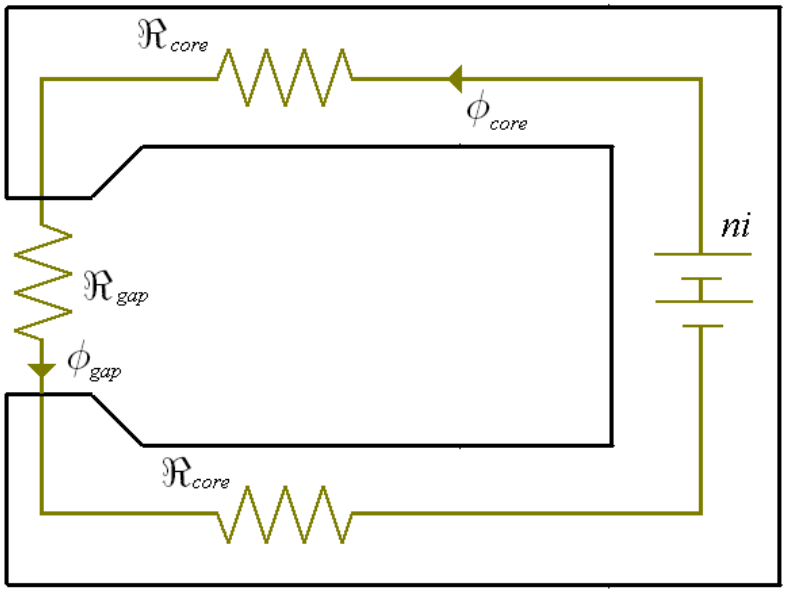

Figure 3.4: Magnetic circuit representation of the MRB

be written in terms of magnetic flux density **B**:

$$\phi = \int_A \mathbf{B} \cdot \mathbf{n} dA = \int_A \mu \mathbf{H} \cdot \mathbf{n} dA \tag{3.3}$$

where **n** is the normal vector to the surface area A.

Eq. (3.3) implies that the magnetic flux is a function of the magnetic field intensity as well as μ and A of the member. Note that **H** in Eq. (3.3) can be obtained by writing the steady-state Maxwell-Ampere's Law (see Eq. 4.1) in an integral form, i.e.

$$\oint |\mathbf{H}| \, dl = ni \tag{3.4}$$

which implies that **H** depends on the *mmf* (or ni) and l of the member. Since maximizing the flux through the MR fluid gap is our goal, Eq. (3.4) can be rewritten as:

$$\oint |\mathbf{H}_{MRF}| \, dl_{MRF} = ni - \oint |\mathbf{H}_{core}| \, dl_{core} - \oint |\mathbf{H}_{disk}| \, dl_{disk} \tag{3.5}$$

where $|\mathbf{H}_{core}|$, $|\mathbf{H}_{disk}|$ and $|\mathbf{H}_{MRF}|$ are the magnitudes of field intensity generated in the magnet core, shear disk and MR fluid respectively and l_{core}, l_{disk}, and l_{MRF} are the length/thickness of the corresponding members. In Eq. (3.5), the negligible losses due to the surrounding air and non-magnetic parts are omitted.

Hence, in order to maximize the flux through the MR fluid, the magnetic circuit should be optimized by properly selecting the materials (i.e. μ) for the circuit members and their geometry (l and A).

3.3 Material Selection

The material selection is a critical part of the MRB design process. Materials used in the MRB have crucial influence on the magnetic circuit (i.e. determines μ) as well as the structural and thermal characteristics. Here, the material selection issue is discussed in terms of the (i) magnetic properties, (ii) structural properties and (iii) thermal properties.

3.3.1 Magnetic Properties of Materials

Before starting the discussion on the material selection for the proposed MRB, the background information regarding the magnetic characteristics of materials is first given here [46]. The main parameter that defines a material's magnetic characteristics is its permeability (μ). It is the ratio between the applied magnetic field intensity (H) and magnetic flux density (B) due to H through the material (See Eq. (3.6)). It is the ability of the material to transfer magnetic flux over itself. In the literature, "relative permeability (μ_r)", which is the ratio between the material's permeability and vacuum's permeability (i.e. $\mu_0 = 4\pi\ 10^{(-7)}$ H/m), is commonly used (see Eq. 3.7). Throughout this thesis, whenever the permeability of a material is mentioned, it refers to its relative permeability.

$$B = \mu H \tag{3.6}$$

$$B = \mu_r \mu_0 H \tag{3.7}$$

Materials are classified in three groups according to their permeability values: i) ferromagnetic materials, ii) paramagnetic materials and iii) diamagnetic materials. Materials that are strongly attracted by the applied magnetic field are ferromagnetic materials. They have permeabilities of higher than 1. Iron, nickel, cobalt and many

alloys of these three materials are examples of ferromagnetic materials. The materials that are attracted weakly by the applied magnetic field are paramagnetic materials and their permeabilities are close to 1, most of the paramagnetic materials have permeabilities between 1 and 1.001. Many salts of iron, rare earth families, platinum and palladium metals, sodium, potassium, oxygen and the ferromagnetic materials above the Curie point[1] are examples of paramagnetic materials. Note that the permeabilities of the above materials are either independent of temperature or decrease with the increasing temperature. The last group of materials is the diamagnetic materials, which are repelled by the applied magnetic field. These materials have a tendency to move toward the weaker field. They have permeabilities smaller than 1. Many of the metals and non-metals other than those mentioned above as examples of the other two categories belong to this group.

In this thesis, the main focus will be on ferromagnetic materials and the term "non-ferromagnetic"will be used to imply the diamagnetic and paramagnetic materials. When a ferromagnetic material is brought closer to a magnetic field source (i.e. a permanent magnet, electromagnet or a current carrying wire), the induced magnetization (B) on the materials can be defined as a function of applied magnetic field (H) and the proportionality coefficient is the magnetic permeability of the material (see Eq. 3.6). In Figure 3.5-(L), a B-H curve is shown for a typical ferromagnetic material and in Figure 3.5-(R), the change of magnetic field permeability of a ferromagnetic material with increasing applied magnetic field intensity is illustrated.

As can be seen from Figure 3.5-(R), permeability is not a constant, but varies with increasing magnetic field intensity. Figure 3.5-(L) shows that as H increases, B approaches to a finite limit due to saturation. This can also be seen in Figure 3.5-(R)

[1] A ferromagnetic material property that is the temperature above which it loses its characteristic ferromagnetic ability

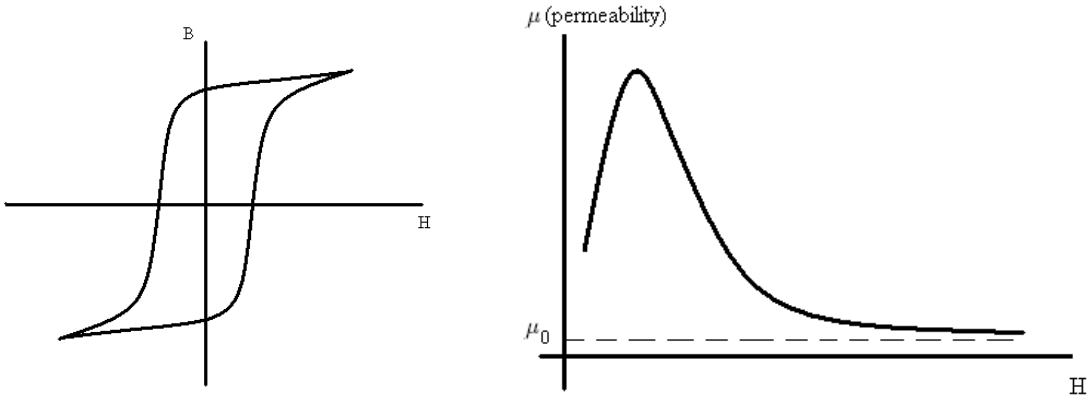

Figure 3.5: B-H curve of a typical ferromagnetic material (L) and varying permeability of a ferromagnetic material with respect to applied magnetic field intensity (R)

as the permeability value converges to that of the vacuum. Thus, once the saturation flux density is reached a ferromagnetic material behaves as a paramagnetic material with permeability close to 1.

In addition to the change with the applied magnetic field intensity, permeability of a ferromagnetic material is also a function of temperature too. It decreases with increasing temperature and also materials lose their magnetic properties after a finite temperature is reached, which is called the Curie Point. Whenever a material is heated up to its curie temperature, its permeability will converge to 1, thus it will behave as a paramagnetic material. For instance, the curie point of iron is around 770℃.

Figure 3.5-(L) also shows another characteristic of ferromagnetic materials known as magnetic hysteresis. When a ferromagnetic material is magnetized in one direction, it does not relax back to its initial starting point after the magnetizing field is removed. Figure 3.6 shows the B-H curve of AISI 1015, low carbon steel, modeled using Hodgdon Model [36, 47]. Magnetic flux generation will grow towards the saturation value through curve 1. If the applied field intensity is subsequently decreased, the flux generation will follow curve 2. When the intensity is zero, magnetic flux has a positive value, which is a residual flux on the material. When the intensity is again reversed, point (a) is reached where residual magnetic field is zero.

In addition to these characteristics, when a ferromagnetic material is magnetized by an external field, its ends carry magnetic poles which cause a magnetic field within the material in the opposite direction of the applied field. Thus, these fields are called *demagnetizing fields*. Also when magnetic field is applied, the dimensions of the material changes too, however it does not exceed a few parts per million. This behavior of ferromagnetic materials is called *magnetorestriction*. Finally, magnetic properties of single crystal materials changes with the direction of measurement,

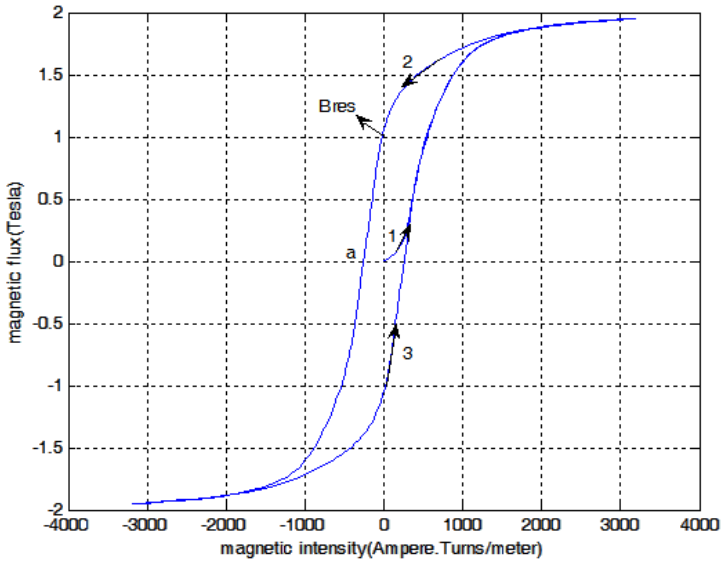

Figure 3.6: Hysteresis cycle of Steel 1015 simulated by Hodgdon Model [47]

which is referred as *magnetic anisotropy*. In many materials, methods of fabrication such as rolling cause regularity in the orientations that will cause anisotropy.

Because of highly non-linear magnetic characteristics of ferromagnetic materials due to hysteresis cycle, saturation, demagnetizing fields, magnetorestriction and magnetic anisotropy, it is hard to measure magnetic properties of a ferromagnetic material accurately and, in general, expensive and highly sensitive equipment is required for such measurements [48].

3.3.2 Selection According to Magnetic Properties

As discussed in the previous section, permeability (μ) of a ferromagnetic material is highly nonlinear and varies with temperature and applied magnetic field intensity (e.g. saturation and hysteresis). In Table 3.1, a few candidate examples of ferromagnetic and non-ferromagnetic materials are listed. As for ferromagnetic materials, there is a wide range of alloy options [48] that are undesirably costly for the automotive brake application. Therefore, a more cost-effective material with required permeability should be selected. In addition, since it is difficult to accurately measure the permeability of materials, in this work, only materials with known properties were considered as possible candidates.

Considering the cost, permeability and availability, a low carbon steel, AISI 1018 was selected as the magnetic material in the magnetic circuit (i.e. the core and disks). Corresponding B-H curve of Steel 1018 with the saturation effect is shown in Figure 3.7.

Table 3.1: Examples of ferromagnetic and non-ferromagnetic materials

Ferromagnetic Materials ($\mu_r > 1.1$)	**Non-Ferromagnetic Materials** ($\mu_r < 1.1$)
Alloy 225/405/426	Aluminum
Iron	Copper
Low Carbon Steel	Molybdenum
Nickel	Platinum
42% Nickel	Rhodium
52% Nickel	302-304 Stainless Steel
430 Stainless Steel	Tantalum
	Titanium

μ_r is the relative permeability

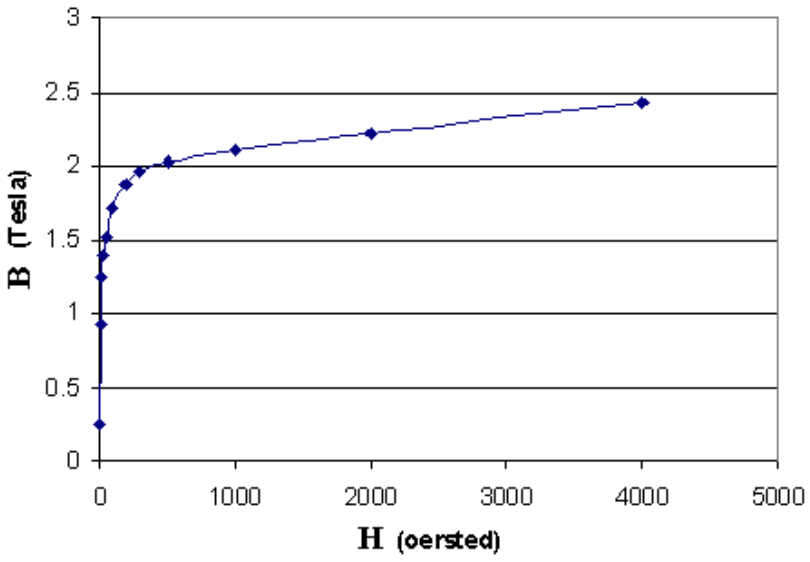

Figure 3.7: B-H curve of Steel 1018 for initial magnetic loading

3.3.3 Selection According to Structural Properties

In terms of structural considerations, there are two critical parts of MRB that must be considered: the shaft which carries the brake and transfers the torque generated by the MRB, and the shear disk where the braking torque is generated. The shaft should be non-ferromagnetic in order to keep the flux far away from the seals that enclose the MR fluid (to avoid from MR fluid being solidified in the vicinity of the seals, see Sec. 3.4 for details). From Table 3.1, it can be easily seen that for the shaft, 304 stainless steel is a suitable material due to its high yield stress and availability. For the shear disk material, low carbon steel was selected since it is a part of the magnetic circuit and its yield stress is high. Since the remaining parts are not under any considerable loading, the choice of material selection in terms of structural considerations is very flexible. In Table 3.2, the properties of 304 stainless steel and 1018 low carbon steel are shown.

Table 3.2: Properties of SS304, STEEL 1018 and Al 6061-T1

Property	SS304	STEEL 1018	Al T-6061
Composition	Cr-18/20%, Ni-8/10.5%, Mn-2%, Si-1%, C-0.08%, P and S	C-0.15/0.2%, Mn-0.6/0.9%, P and S	Mg-0.8/1.2%, Si-0.4/0.8%, Cu-0.15/0.4%, Fe, Cr, Ti and Zn
Tensile Strength (MPa)	515	634	124
Yield Strength (MPa)	205	386	55.2
Hardness Rockwell B	88	197	30
Density (kg/m^3)	8000	7700-8030	2700
Modulus of Elasticity (GPa)	193	190-210	68.9
Thermal Conductivity (W/m-K)	16.2	51.9	180
Specific Heat (J/kg-K)	500	486	896

3.3.4 Selection According to Thermal Properties

Another factor that makes the material selection an important step is the thermal properties of the materials. Due to the temperature dependent permeability values of the ferromagnetic materials and the MR fluid viscosity, heat generated in the actuator should be removed as quickly as possible. In order to understand the heat flow, Eq. (3.8) below which is the law of conduction, *Fourier's Law*, is briefly considered. This equation is a constitutive equation that depends on the thermal conductivity k_{con}:

$$\frac{\partial Q}{\partial t} = -k_{con} \oint \nabla T dS \tag{3.8}$$

where Q is the heat transferred, ∇T is the temperature gradient between the ambient and heat source and S is the area where the heat flows through. According to Eq. (3.8), in order to increase the rate of heat transfer from the MRB, the ambient temperature can be lowered which will increase temperature gradient, ∇T. In order to decrease the ambient temperature, a cooling mechanism should be introduced. Possible mechanisms that can be used for heat removal from the brake will be discussed in Sec. 3.5.

In addition, in terms of thermal considerations, in order to increase the heat removal from the MRB, a material with high conductivity and high convection coefficient has to be selected as the material used for the non-ferromagnetic brake components. Aluminum (Al 6061-T1) is a good candidate material based on the thermal considerations. In Table 3.2, thermal properties of stainless steel 304, low carbon steel 1018 and Al 6061-T1, which are the materials that were selected to be used in the MRB prototype, are presented.

3.4 Sealing

Sealing of the MRB is another important design criterion. Since the brake employs an MR fluid, it has to be sealed properly against a possible leakage, which will cause the loss of braking. Because MR fluids are highly contaminated due to iron particles which makes sealing a critical issue. In addition, in the case of the dynamic sealing required between the static casing and the rotating shaft, there is a greater possibility of sealing failure when the MR fluid is repetitively solidified (due to the repetitive braking) around the vicinity of the seals.

In order to decrease the risk of sealing failure, the dynamic seals have to be kept away from the magnetic circuit in the brake. This will decrease the magnetic field intensity that is generated in the vicinity of the seals during braking, thus avoiding the on/off cycle of the MR fluid. Also, since the fluid is contaminated, surface finishes and the sealing method itself are of a great importance.

In this work, the dynamic seals were kept away from the magnetic circuit by introducing a non-ferromagnetic shaft and shear disk support outside the circuit which holds the magnetic shear disks (see Figure 3.1). Also the surface finishes were improved and the tolerances were kept tight for better interface between the seals and the counterpart surfaces. In Figure 3.8, the sealing types used in the MRB and their locations are shown. In the MRB proposed, Viton O-rings were used for both static and dynamic applications. In addition, as a sealant, Loctite 5900® Flange Sealant, was also used.

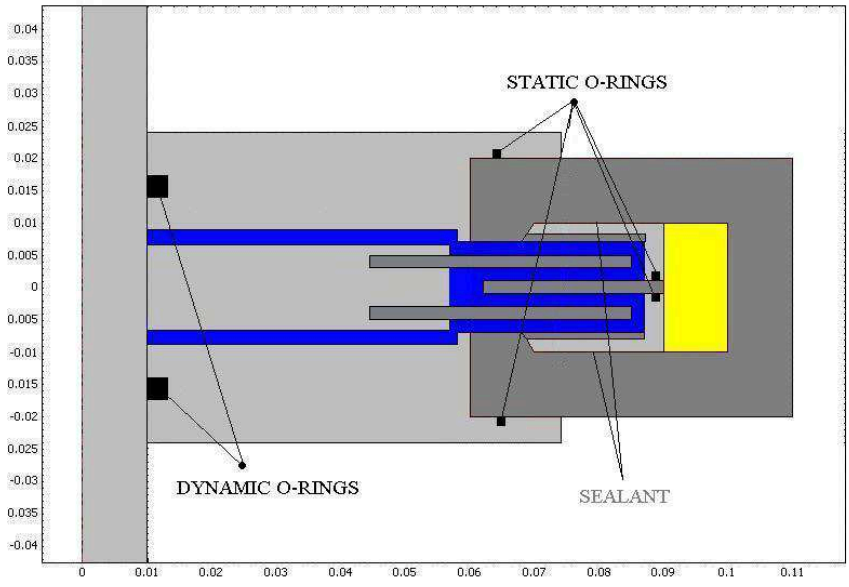

Figure 3.8: Different seals on proposed MRB design

3.5 Cooling

The heat flow within the basic MRB configuration, which was presented in Figure 1.2, was investigated by Falcao da Luz [38]. Transient and steady state heat flow analyses were done assuming that the MR fluid employed was MRF-132DG® and the heat was removed by forced convection from the casing of MRB as well as the conduction between the brake components. A braking schedule, that consists of 15 cycles each comprising a 28 s acceleration period followed by a 0.3 g deceleration from 120 kph to a full stop, was adopted and according to this study, after 15 cycles, the temperature within the brake reached 100℃ which is still in the operating range of the selected MR fluid. But, with more severe repetitive braking, the temperature will exceed the operating range eventually.

In this work, heat flow analysis was not included in the FEA, as the main focus lied on the braking torque generation capacity of the MRB. However, an effective and fast heat removal from the brake is crucial, since the MR fluid properties (i.e. viscosity) and the magnetic properties (i.e. μ) of the materials employed are dependent on the temperature. Especially, due to the existence of a carrier fluid in MR fluids, their operating range (see Sec. 3.10) is quite limited. In addition, in braking applications, the kinetic energy of the vehicle is transformed into heat within brakes and a CHB can reach over 600℃. The same will be valid for the MRB as well, and thus the heat has to be removed from it as fast as possible.

There are various methods of cooling the brakes which can be divided into two categories: active and passive cooling. As passive cooling, in addition to selecting thermally conductive materials with high convection coefficients (see Sec. 3.3.4), fins can be introduced which will increase the convection surface on the MRB and this method of cooling was suggested in [38]. However, these methods will not increase

the heat flux considerably. Therefore, an additional active cooling system should be introduced. In active cooling, the heat flux is increased by the introduction of a forced heat transfer fluid (i.e. water, air, coolant, etc). The term "forced" is used to imply that, in active cooling, additional components such as pumps and fans are used to help the heat transfer from the system to the ambient environment by circulating the heat transfer fluid between these mediums. The analyses in [38] were carried out by assuming that there was forced convection between the brake casing and the ambient air when the vehicle is moving.

For the MRB heating problem, since this is an automotive application, similar to an active engine cooling system, a water cooling system can be included to the design. In addition, a fan can also be attached to the shaft which will cool the MRB. Another method that can also be used is to consider the MR fluid itself as a cooling fluid. An MR fluid reservoir for each brake can be included into the system which has an active cooling system introduced. The idea is similar to the way of cooling the water, that cools the engine, in the radiator. Since the main concern is the temperature of the MR fluid, a reservoir will be efficient to keep the MR fluid temperature within the operation temperature. But, on the other hand, a reservoir will need a pump or an active system that helps the MR fluid circulation and introduction of new components will increase the overall weight of the actuator as well as the cost of the brake.

But as mentioned previously, since the main concern of this thesis lies in the brake torque capacity of the MRB for the automotive application, the effects of adding active or passive cooling systems were not studied. This remains as an important future work that must be addressed (see Sec. 6.2).

3.6 Working Surface Area

As mentioned previously, a working surface is the surface on shear disk(s) where the MR fluid is actuated by applied magnetic field intensity. Basically, it is the surface where the magnetic shear, τ_H, is generated, thus the braking torque. Working surface is another important design factor. Since the braking torque is generating on this surface, torque has a direct dependence on the surface area. From Sec. 2.2, Eq. (2.10) shows that the braking torque is the area integral of the shear of the MR fluid. If the surface area is increased then generated torque would be increased too. There are multiple ways to increase the working surface area.

The first way to increase the working surface area is to enlarge the surface area of the pole caps. But by enlarging it, the flux will be distributed over the cross section and in the working surface, there will be less magnetic flux density. However, the main concern is the change in the braking torque generated, so the flux flow over the fluid, not over the surface area of the pole caps. Due to nonlinear behavior of magnetic properties, one cannot conclude that the braking torque will increase by enlarging pole caps' surface area and it will decrease by reducing it. Therefore, the surface area of the pole caps has to be optimized for maximum braking torque generation by using proper optimization method and constraints.

Another way of enlarging the working surface is to modify the magnetic circuit itself. As was mentioned in Sec. 3.2, in order to modify the magnetic circuit, the materials used, the configuration of the magnetic circuit and the dimensional design parameters can be changed. Since there are not many material in the literature with known (published) detailed magnetic properties, changing the material makes the subsequent MRB design and analysis difficult. However, by modifying the configuration of magnetic circuit and changing the dimensional design parameters, magnetic

flux generated can be focused onto fluid and the working surface area can be enlarged.

One must be careful when modifying the basic configuration of the magnetic circuit. In relation to the working surface area issue, the alignment orientations of the iron particles in the MR fluid must be considered. For more effective braking torque generation, a magnetic circuit has to be designed in such a way to align the iron particles in the MR fluid perpendicular to the working surfaces. Figure 3.9 and Figure 3.10 shows three cases of possible particle alignment in the MR fluid. Figure 3.9 shows the distribution of the iron particles without magnetic field application and thus no angular velocity. The static casing is the upper working surface and the lower working surface is the shear disk surface. Figure 3.10 represents two different cases when the external magnetic field is present. In Figure 3.10-(L), the static casing and the shear disk are made of non-ferromagnetic materials. Since the permeability of the MR fluid is higher than that of the surrounding materials, particles will align parallel to the working surfaces due to the parallel flux flow through the MR fluid gap. Recall that the magnetic flux will flow over a medium in which the permeability is higher. This parallel alignment of the iron particles will result in layers of parallel chains throughout the MR fluid gap thickness. Since the bond between the layers is weak, they will be subjected to slipping during braking.

However, when ferromagnetic materials are used for static casing and the shear disk, the magnetic flux will prefer to flow through them instead of the MR fluid. In order to complete the magnetic circuit, the flux will flow perpendicular to the static casing and shear disk surfaces which will result in a perpendicular alignment of the iron particles. This can be seen in Figure 3.10-(R), the resistance against the motion of the shear disk will be increased due to the formation of the perpendicular chains. In this case, slipping between the layers would not occur.

Another way that helps to increase the working surface area is the introduction

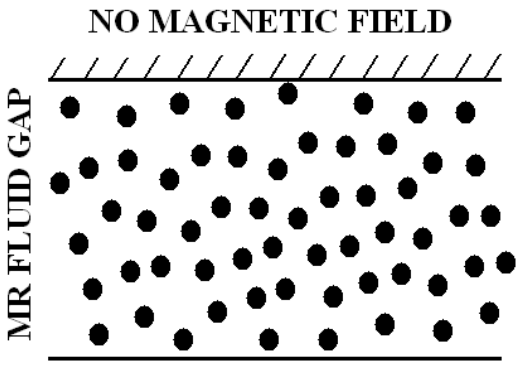

Figure 3.9: Iron particle alignment without magnetic field application

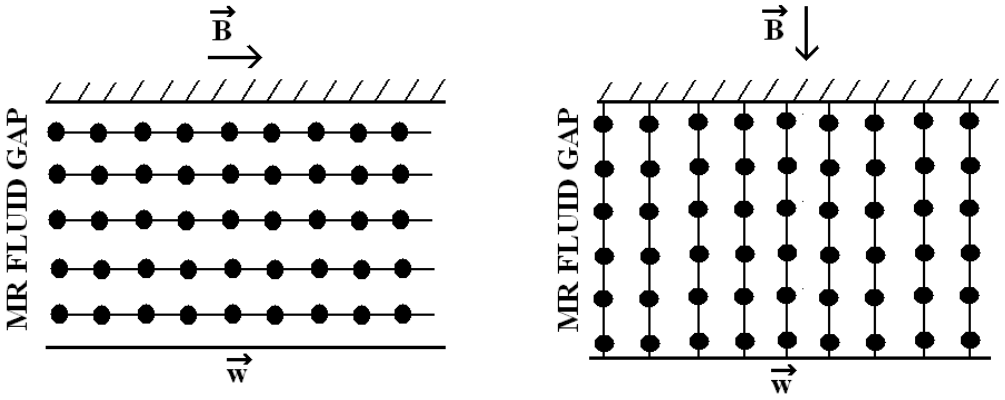

Figure 3.10: Alignment of iron particles with magnetic field application between non-ferromagnetic casing and shear disk (L) and ferromagnetic casing and shear disk (R)

of additional shear disks, which will be discussed in more detail in Sec. 3.9.

In our MRB design, the dimensional parameters were optimized for higher braking performance and also ferromagnetic layers were installed on the static casing in order to achieve the perpendicular alignment of the iron particles in the MR fluid when the external magnetic field is applied.

3.7 Viscous Torque Generation

The gap between the stator and the rotor is filled with the MR fluid, which generates some amount of braking torque, i.e. viscous torque, even without the magnetic field application. The viscous torque is generated due to the viscosity of the MR fluid, which cannot be removed completely. However, it can be decreased to a reasonable value.

There are multiple ways to decrease the amount of viscous torque generated. The very first thing that should be done is to select an MR fluid with a low viscosity value, which will be addressed in Sec. 3.10. Viscous torque can also be decreased by decreasing the shear rate value. Eq. (2.11) gives the shear rate as a function of fluid velocity and the thickness of the gap, with the assumptions of no slip conditions, thin fluid gap thickness and linear velocity distribution of fluid flow over the fluid gap thickness. This equation tells us that, in order to decrease the shear rate, the thickness of the gap, which is filled with the MR fluid, should be increased.

In order to show the effect of a change in the fluid gap thickness on the viscous torque generation, the MR fluid flow was briefly studied. A laminar Couette flow analysis was carried out in order to simulate the flow between the static casing and a rotating disk. A Coquette flow, shown in Figure 3.11, is a simple viscous parallel plate flow of a Newtonian fluid, developed between a stationary plate and a moving

plate. Newtonian fluid is the one in which shear stress is distributed proportionally to the velocity gradient in the direction perpendicular to the direction of shear plane.

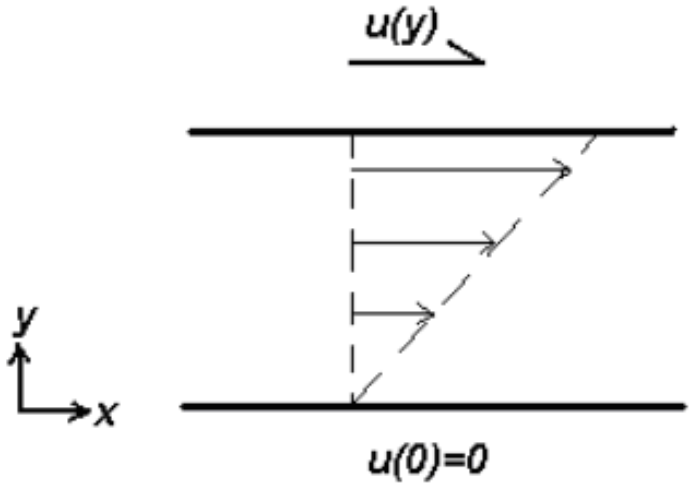

Figure 3.11: Couette flow

For this type of flow, a shear stress is generated between the fluid and the plate, and this shear stress is directly related with the viscosity of the fluid. Basically, fluid resists the flow in the direction of motion and this resistance is a function of the viscosity and derivative of the velocity with respect to thickness. This relationship is shown in Eq. (3.9) for the geometry specified in Figure 3.11. Moreover, for calculating the braking torque, the shear stress is multiplied by the area and the moment arm. In Eq. (3.10), the general torque equation in cylindrical coordinates is given (similar to Eq. (2.15) defined for the MRB).

$$\tau = \mu_p \frac{du}{dy} \tag{3.9}$$

$$T = \int_j^z \int_0^{2\pi} \tau r^2 d\theta dr \tag{3.10}$$

where u is the linear velocity in x direction, μ_p is the plastic viscosity, and θ is the angle that the radius makes with the horizontal.

Figure 3.12 shows the actual picture of the problem, in which a disk rotating within a static enclosure. As it can be seen from the figure, there are two types of flow motion: one is in the radial direction and the other is in the tangential direction. In addition, the flow motion does not depend on the angle, θ, which implies that the motion is same everywhere on an arbitrary circle in the fluid.

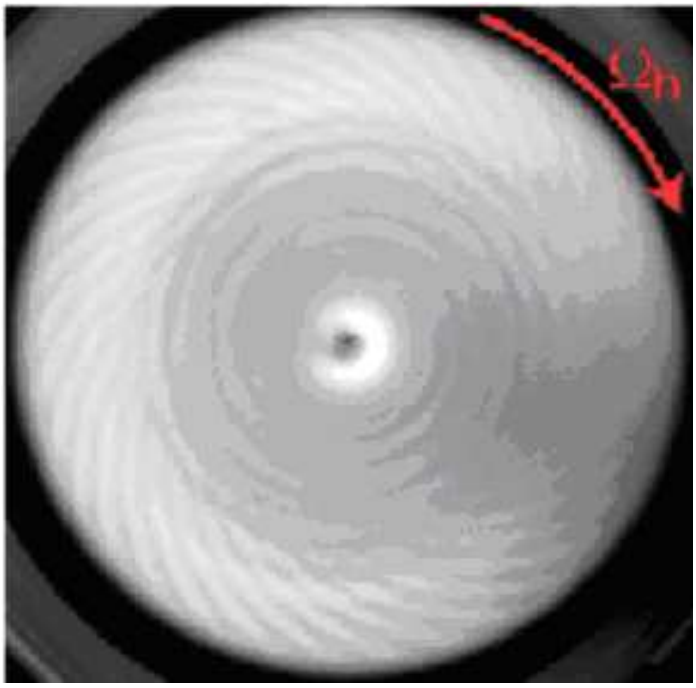

Figure 3.12: Experimental flow patterns developed by a rotating disk within a static enclosure

The following assumptions were made in regards to the MR fluid flow problem:

1. Newtonian Flow.
2. Steady and incompressible flow.
3. No radial flow.
4. No change of velocity in the tangential direction.
5. No pressure gradient and gravitational effects on the flow.

With the above assumptions, the flow problem becomes a 1-D problem:

$$\mu_p \frac{d^2u}{dy^2} = 0 \tag{3.11}$$

which is an idealized case that should be sufficient for our purpose. By solving the above Navier-Stokes equation, the flow profile between the stationary casing and the rotating disk is shown in Figure 3.13. This is the flow that is expected for the Couette Flow.

With the above velocity profile between the stationary and the rotating parts, the shear stress and the torque can be calculated by just using the slope of the curve and the viscosity. Lord Corporations's MRF-132DG® was selected and used in the flow analysis, which has the plastic viscosity of 0.09 Pa-s. Figure 3.14 shows the change in the viscous torque with respect to the changing fluid gap thickness. In this plot, the results were multiplied by a factor of 4 to obtain the total sum of the viscous torque when 4 MRBs are used in a car. According to the plot, for a gap of 1 mm between the static enclosure and the disk, a viscous torque of around 13 Nm is generated purely due to the viscosity of the MR fluid in each brake (around 50 Nm for 4 brakes) while the car is moving at 60 kph. An additional load that the engine has to overcome while the car is traveling.

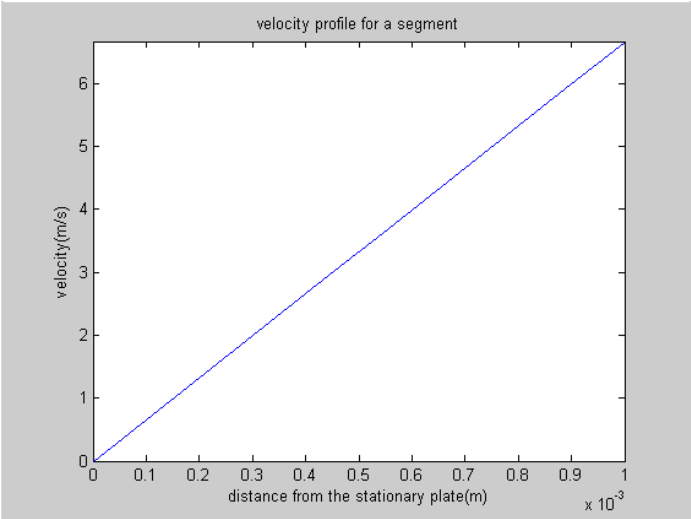

Figure 3.13: Velocity profile for a segment away from 0.12 m from the center of the disk

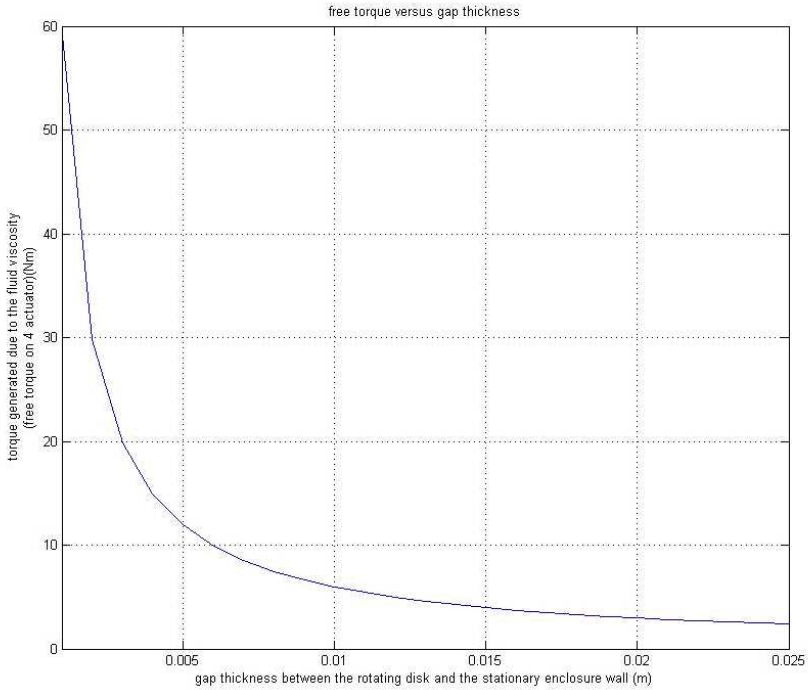

Figure 3.14: Viscous torque versus the gap thickness of MR fluid (at 60 kph)

In order to decrease the amount of viscous torque that impedes with the free shaft rotation of MRB, MR fluid with a low viscosity value was selected, and the fluid gap thickness was optimized along with the other dimensional parameters for better brake performance.

3.8 Applied Current Density

The electromagnet coil is another important design criterion, as it is the source (i.e. the magnetomotive force or *mmf*) in the magnetic circuit. The current density that can be applied to the electromagnet coil is limited, which depends on the cross-sectional area of the wire, its material, and the saturation flux densities of the magnetic materials used in the MRB. When the saturation flux value of a magnetic material, especially that of the electromagnet core material, has been reached, it will behave as non-magnetic material (i.e. μ_r becomes 1), affecting the corresponding reluctance in the magnetic circuit which will result in a change in the magnetic circuit, and consequently the amount of flux flow through the MR fluid. Thus, it is beneficial to keep the flux in the unsaturated region for that material.

In order to maximize the amount of applied current density, the dimensional space where the coil is located needs to be optimized along with the other dimensional parameters. In addition, a wire size, with the highest current density capacity was selected. In order to find the most efficient wire in terms of the current density carrying capacity, a coil with a winding configuration of Figure 3.15 was studied. By drawing an equilateral triangle, the effective cross sectional area of the wire can be calculated within the triangular area and the corresponding current density application capacity was calculated by dividing the *mmf* by the calculated triangular area. The *mmf* was calculated by using the maximum current carrying capacity of the wire.

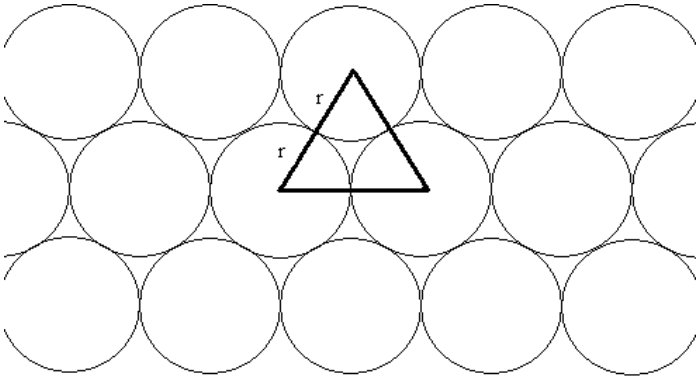

Figure 3.15: Wire configuration in a coil

Table 3.3 shows the corresponding current densities that can be applied to the coils made of different sizes of wires. According to this study, the most efficient wire size is the AWG 21. More current density can be applied to the MRB using this wire size, which means that the magnetic field intensity generated within the brake will increase. Note that, from Eq. (2.14), the amount of the magnetic torque generated will be increased with the increasing magnetic field intensity. Therefore, in this work, the AWG 21 size copper wire was used to wind the coil of the MRB's electromagnet.

3.9 Additional Disk Attachment

In order to increase the amount of braking torque generated in the brake, additional brake disks can be attached to the shaft to increase the working surface area. By attaching additional disks, additional working surfaces would be introduced (see Sec. 3.6 for other ways to increase the working surface area). In Figure 3.16, two brake cross sections are shown: one with only one shear disk attached to the shaft and the other

Table 3.3: Current densities for coils of wires with different sizes

awg gauge	diameter (mm)	ohms per km	current density (A/mm^2)
7	3.665	1.634	2.587
8	3.263	2.060	2.610
9	2.905	2.598	2.607
10	2.588	3.276	2.594
11	2.303	4.132	2.619
12	2.052	5.208	2.558
13	1.828	6.569	2.563
14	1.628	8.282	2.578
15	1.450	10.443	2.588
16	1.290	13.172	2.574
17	1.150	16.609	2.538
18	1.023	20.942	2.543
19	0.911	26.407	2.508
20	0.812	33.292	2.630
21	0.723	41.984	2.653
22	0.645	52.939	2.561
23	0.574	66.780	2.563
24	0.510	84.197	2.564
25	0.454	106.173	2.561
26	0.403	133.856	2.564
27	0.360	168.821	2.565
28	0.320	212.872	2.556
29	0.287	268.402	2.559
30	0.254	338.496	2.550
31	0.226	426.728	2.562
32	0.203	538.248	2.553
33	0.180	678.632	2.565
34	0.160	855.752	2.533

one with two disks attached. In the latter, the working surface area is increased but also the magnetic resistance (reluctance) in the circuit is increased.

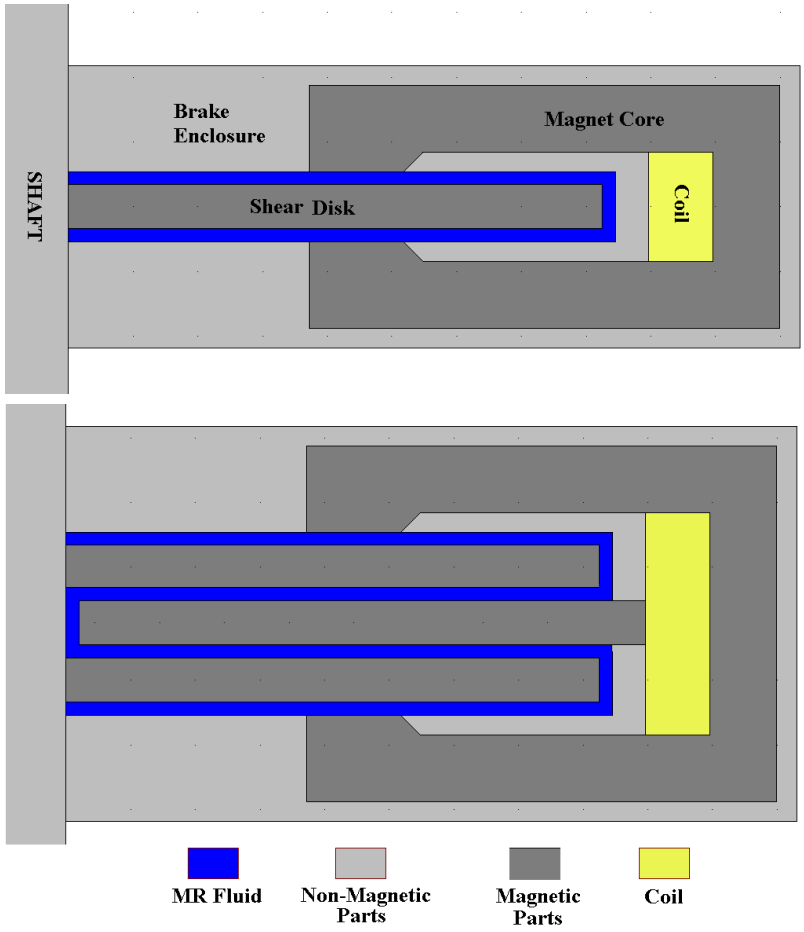

Figure 3.16: Surface plots with one (top) and two (bottom) rotating shear disks attached to the shaft

The braking torque generated is calculated by using Eq. 2.10, integrating the shear stress over the working surface area. The working surface area in Figure 3.16-(bottom) is doubled and the amount of torque generated in two disk design is expected to be roughly twice as much as the torque generated in the one disk design. Due to

the nonlinearity of the material properties and the dependence on the geometry, the amount of change in braking torque can only be estimated accurately using an adequate finite element analysis. Hence, the proposed MRB has two shear disks ($N = 2$) attached to the shaft for higher braking torque generation.

3.10 MR Fluid Selection

There is a number of commercially-available MR fluids sold by Lord Corporation. In terms of selecting the fluid that is most suitable for braking purposes, there are multiple properties that have to be considered. Viscosity of the fluid without magnetic field application is one of those properties. Since the gap between the stator and rotor is filled with the fluid, viscous torque is present in the MRB. Thus in order to keep the viscous torque low, a fluid with a low viscosity has to be selected.

Another important property of MR fluid is the operating temperature range. Since we are considering a brake actuator, the kinetic energy of the car will be transferred as heat in the MRB, and it will heat up while braking. Since the magnetic properties of the materials in the MRB and the MR fluid viscosity depends on the temperature, the fluid with a broader operating temperature range has to be selected in order to maintain the braking performance at higher operation temperatures.

The shear stress gradient with respect to the applied magnetic field intensity is another important property of the MR fluid. By keeping the shear stress gradient high, the amount of braking torque that could be generated by the brake will also increase.

According to Falcao da Luz [38], MRF-132DG® is the best candidate for the automotive braking application due to its broad operating temperature range (-40 to 130℃). However, the shear stress gradient of MRF-132DG® is lower than that

of MRF-241ES® which has an operating temperature range from -10 to 70℃. In Table 3.4, the properties of MRF-132DG® and MRF-241ES® are summarized and the relationships between the magnetic field intensity and the shear stress generated for both fluids are shown in Figure 3.17.

Table 3.4: Properties of MRF-132DG® and MRF-241ES®

Property	**MRF-132DG®**	**MRF-241ES®**
Base Fluid	Hydrocarbon	Water
Operating Temperature	-40 to 130℃	-10 to 70℃
Density	3.09 g/cc	3.8-3.92 g/cc
Color	Dark gray	Dark Gray
Weight Percent Solid	81.64 %	85 %
Coef. of Thermal Expansion (Unit Volume per ℃)		
0 to 50℃	5.5e-4	0.226e-3
50 to 100℃	6.6e-4	
100 to 150℃	6.7e-4	
Specific Heat at 25℃	0.80 j/g℃	0.94 j/g℃
Thermal Conductivity at 25℃	0.25-1.06 w/m℃	0.85-3.77 w/m℃
Flash Point	> 150℃	> 93℃
Viscosity		
slope between 800 Hz and 500 Hz at 40℃	0.09(± 0.02)Pa-s	
10 Hz		10.8 ± 1.5 Pa-s
50 Hz		2.2 ± 0.4 Pa-s
k	0.269 Pa-m/A	0.467 Pa-m/A
β	1	1

However, even though the shear shear generation capacity of MRF-132DG® is approximately only a half of that of MRF-241ES®, MRF-132DG® was chosen for having a broader temperature range. In addition, MRF-132DG® does not contain water which may result in corrosion of the MRB.

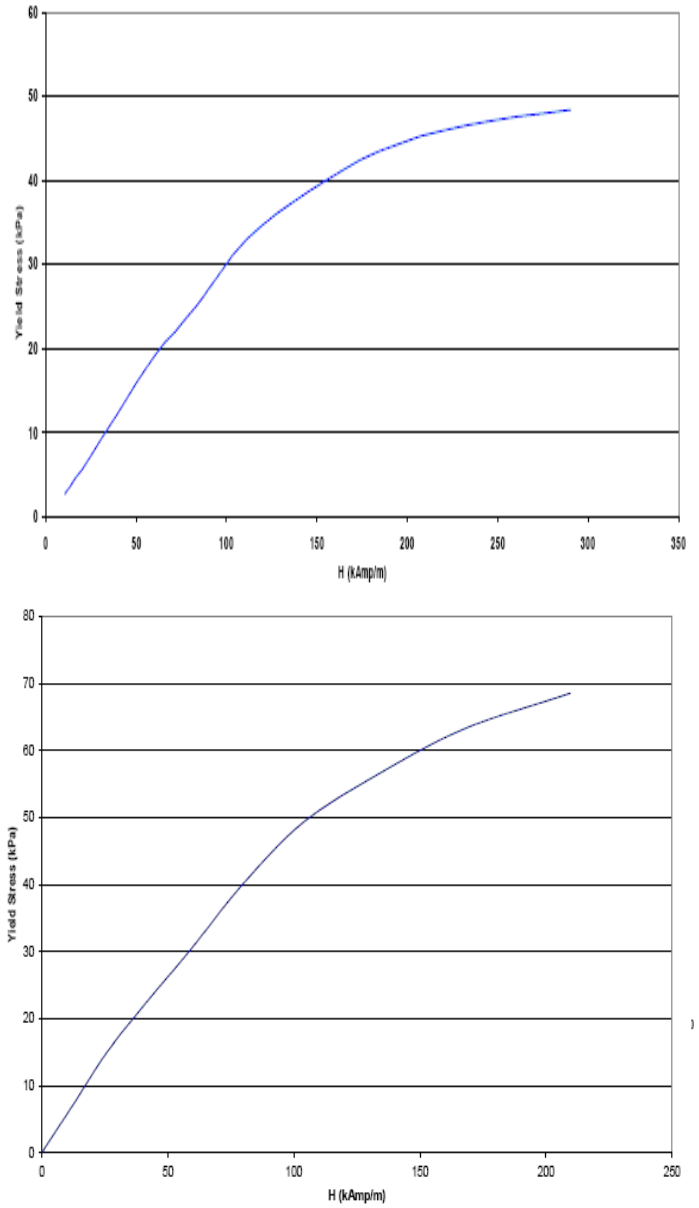

Figure 3.17: Shear stress versus magnetic field intensity for MRF-132DG® (top) and MRF-241ES® (bottom)

Chapter 4

FEA and Design Optimization

The analytical MRB model was derived in Sec. 2.2. As shown by Eq. (2.13), the total braking torque T_b generated is a function of the material properties (i.e. viscosity of the fluid, k and β coefficients) and the magnetic field intensity distribution on the MR fluid (H_{MRF}). While the material properties are given by the manufacturer's specifications, however, the magnetic field intensity distribution has to be calculated within MRB. In order to obtain this, a finite element model (FEM) of the MRB was created and using nonlinear magnetic properties of materials employed, the magnetic field distribution within the MRB was calculated.

In this chapter, the FEM generated for the MRB is presented. In addition to the generation of the FEM, the finite element software used also described. The resulting magnetic flux and magnetic field intensity distribution plots for the selected design shown in Figure 3.1 are also included in this chapter.

After the FEM was created for the proposed MRB design, it was optimized for the maximum braking torque generation and minimum weight. For the optimization process, an MRB optimization problem was defined with a corresponding objective

function and a set of constraints. Then, existing optimization methods were used in order to solve for the optimum MRB dimensional design parameters.

4.1 Finite Element Model of MRB

To solve Eq. (2.13), the magnetic field intensity distribution in the MRB has to be calculated. For this purpose, a finite element analysis (FEA) was carried out using a commercial FEA package, COMSOL Multiphysics®. The following governing magnetostatic equations [49], that were derived from Maxwell's equations (see Appendix A), are used by the COMSOL Electromagnet Module:

$$\nabla \times \mathbf{H} = \mathbf{J} \tag{4.1}$$

$$\nabla \cdot \mathbf{B} = 0 \tag{4.2}$$

where $\mathbf{H}$ is the magnetic field intensity, $\mathbf{B}$ is the magnetic flux density and $\mathbf{J}$ is the electric current density. By solving these equations over a defined domain with proper boundary conditions, the magnetic field intensity distribution ($\mathbf{H}$) generated by the modeled MRB can be calculated. Subsequently, the braking torque in Eq. (2.14) can be calculated.

In order to solve the above magnetostatic equations, a 2-D MRB finite element model (FEM) was created. The FEM is a quasi-static magnetic model, which simulates the in-plane induction currents and vector potentials, needed to obtain the magnetic field intensity distribution ($\mathbf{H}$) over the defined MRB geometry. First, the geometry of the proposed MRB was generated using the sketch function in COMSOL and the nonlinear material properties of the MR fluid and AISI 1018 were defined as functions of the magnetic flux density $\mathbf{B}$. Then, a magnetically isolated boundary

that includes the MRB geometry was selected. After the mesh was generated, the FEM was solved using a parametric nonlinear solver and the magnetic field distribution onto the MR fluid (i.e. H_{MRF} which is equal to the magnitude of the magnetic field distribution, $|\mathbf{H}|$) was obtained. Finally, the braking torque in Eq. (2.13) was calculated using a boundary integration post processing function in COMSOL that integrates the shear, that is calculated by the magnetic field intensity distribution, over the shear disk surfaces.

The FEM accounts only for the magnetic field distribution. Fluid flow dynamics and heat transfer models were not included in the FEM. In Figure 4.1 and Figure 4.2, the simulations of the magnetic field intensity and the flux density in the MRB are shown.

4.2 Optimization Problem Definition

As a next step, the revised design in Figure 3.1 was optimized for higher braking torque and lower weight. In setting up an optimization problem for the MRB, a cost function was defined by including the braking torque and the weight as functions of the magnetic circuit design parameters, (see Figure 3.2). The objective function of the MRB optimization problem is defined as:

$$f(\mathbf{d}) = W - T \tag{4.3}$$

where $\mathbf{d} = [d_1, d_2, ..., d_{12}]^T$ is the design variable vector that consists of the dimensional parameters shown in Figure 3.2, W(N) is the weight of the actuator and T(Nm) (equal to T_H in Eq. (2.14)) is the braking torque generated due to applied magnetic field.

But there is a conflict between terms since these terms have different units in

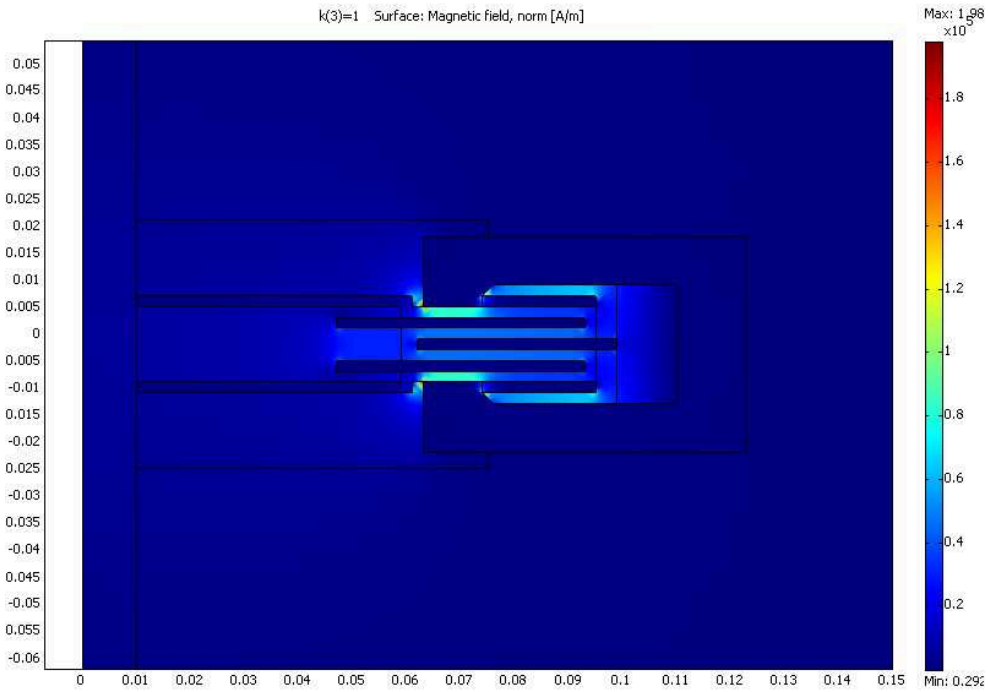

Figure 4.1: Magnetic field intensity distribution Plot generated by COMSOL

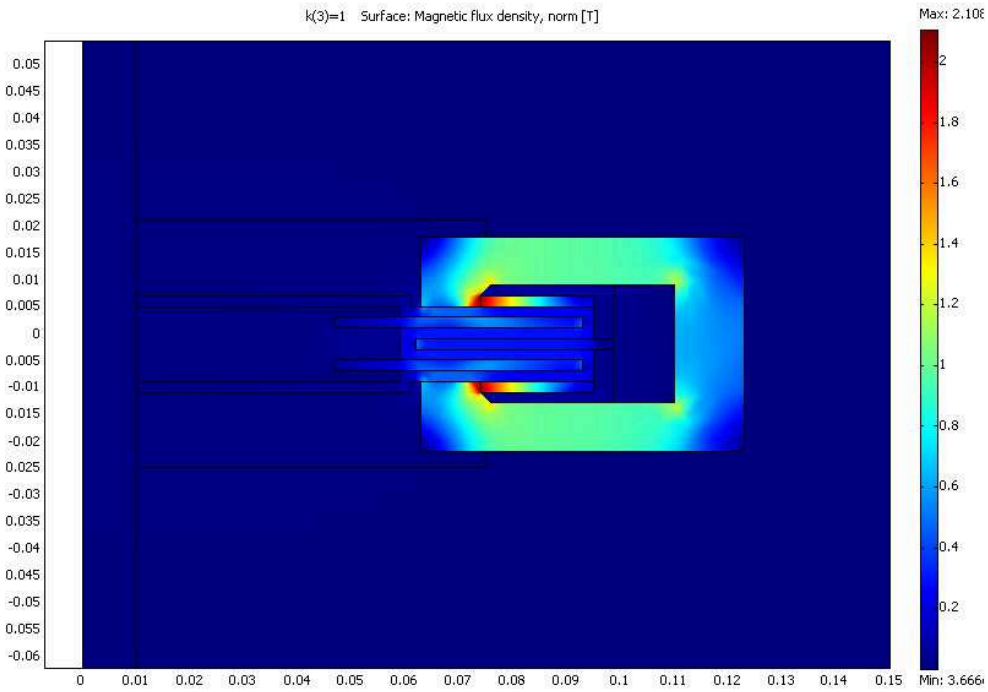

Figure 4.2: Magnetic flux density plot generated by COMSOL

Eq. (4.3). Higher term will dominate over the other and the minimum value and the optimized variables will be deviated from the exact solution. In order to overcome this problem a reference value can be set for each function separately and dividing the terms by the reference will give dimensionless values which can be compared. Thus, the cost function becomes:

$$f(\mathbf{d}) = \frac{W}{W_{ref}} - \frac{T}{T_{ref}} \tag{4.4}$$

where the values with the subscript "*ref*" are the reference values for the functions.

In this form, the cost function is defined and can be optimized. But if one of these functions, weight or braking torque, is wanted to be dominated over the other in the optimization process, weighting coefficients should be introduced. Every term will be multiplied by coefficients and these coefficients are estimated in accordance with the importance of the term in the optimization process. For MRB optimization problem, the braking torque generated has a considerably important role compared to the weight of the actuator, because main goal of the optimization process is to find the design which can generate maximum torque in accordance with the constraints. Therefore, the coefficient of weight function should be less than the coefficient of the braking torque function. Final form of the optimization function will be:

$$\texttt{Minimize} \ : f(\mathbf{d}) = k_W \frac{W}{W_{ref}} - k_T \frac{T}{T_{ref}} \tag{4.5}$$

$$k_W + k_T = 1 \tag{4.6}$$

$$\texttt{subject to} \ : W < 18 \tag{4.7}$$

$$d_{brake} < 240 \tag{4.8}$$

where k_W and k_T are the weighting coefficients. The FEM was used to obtain W and T in the cost function for various brake designs. The block diagram in Figure 4.3

shows the process of calculating W and T via COMSOL in the cost function for an arbitrary design.

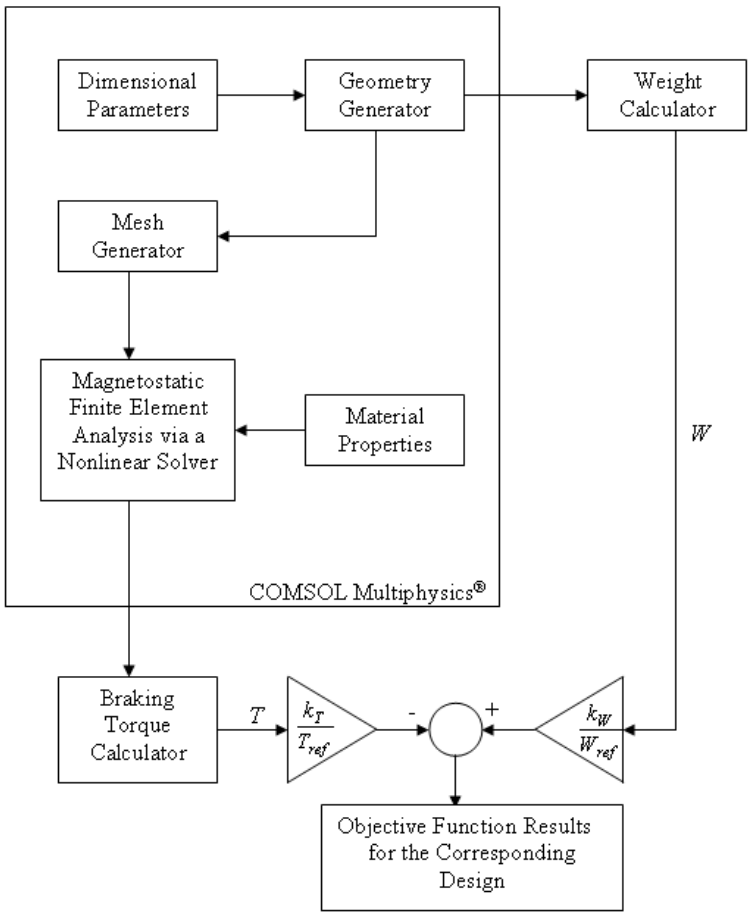

Figure 4.3: Process of computing the cost function for a random design

In order to solve the objective function, k_w was set to be 0.1 and k_T was set to be 0.9, as the maximum torque generation is of our primary concern. In addition, the reference weight value was obtained considering the overall system weight of the CHB that consists of the on wheel components as well as the extra weight contributed by

the hydraulic components: the master cylinder, brake fluid lines, and pump. Since an MRB would not have these extra components, each MRB can potentially have heavier on-wheel weight than that of a CHB. Moreover, since the braking torque generated by the proposed configuration of the MRB is comparably less than that of the CHB, T_{ref} was selected to be 20 Nm. This reference torque value was selected by checking a number of random designs which satisfied the constraints.

As the constraints for the optimization problem, the weight of the actuator was set to be smaller than the weight of the CHB, i.e. $W < 18$ kg. Since the brake should fit into a standard automobile wheel, the diameter of the MRB is set to be smaller than the inner diameter of the wheel. The diameter constraints for various sizes of wheels are shown in Table 4.1, for example, 13" wheel, the inner diameter is 240 mm, thus $d_{brake} < 240$ mm.

Table 4.1: Inner diameters of wheels of different sizes

Wheel Size (in.)	**Inner Wheel Diameter (mm)**
13	240
14	260
15	278
16	308
17	325
18	355

4.3 Optimization Methods Used

The MRB objective function and constraints are defined in previous section. As a next step, optimization methods that were used were selected. Before introducing the methods selected in order to solve the MRB optimization problem, brief back-

ground information about the optimization methods in general will be beneficial to understand the method selection process.

Optimization methods can be classified as gradient based methods, random search algorithm and iteration search algorithms which are the combinations of random search and gradient based methods. Gradient based algorithms are capable of finding the exact optimum solution since the gradient of the cost function is used to determine the search direction and step sizes. Gradient based optimization algorithms are started with an initial guess. Using the gradient information, the search direction and the step size are calculated and according to them, the optimum can be found.

Unlike gradient based algorithms, random search methods do not need the gradient information in order to determine the iteration direction. Iterations are made according to a random search algorithm defined for every method separately. Since the search is random, finite number of iterations is made. This results in a solution which is different from the exact optimum solution. For a random search algorithm, a domain of optimization variables has to be defined and the algorithm will search the space for the minimum value of the cost function defined as a function of optimization variables specified.

Although gradient based methods give the exact minima, that minima may not be the global minima depending on the nonlinearity of the cost function and number of local minima's and maxima's. Since gradient methods will converge to a minimum which is close to the initially defined point, it could converge to a local minimum instead of the global minimum. Therefore, in order to solve MRB problem, a random search algorithm was used.

Among different methods of random search, simulated annealing method [50, 51] was selected in order to solve the MRB optimization problem. There are also other methods like neural nets, iterated searches, genetic algorithmsetc, but simulated an-

nealing was selected due to its statistical guarantee to converge global optimum point and also it was selected due to its simplicity. SA simulates the statistical crystal growth process using material annealing to converge to the absolute minimum internal energy configuration of the crystal. With enough given time to run and enough number of iterations, such algorithm is capable of finding the global optimum for a nonlinear problem.

But since this method is a random search method, finite number of iterations is made and because of that, the design that is going to be found by simulated annealing method is not going to be the exact global minimum. In order to find the exact global optimum, a gradient based algorithm was run after solving the problem by using a random search algorithm, simulated annealing form MR Brake problem.

After solving the problem by using simulated annealing, results of the algorithm were used to initiate a gradient based method, which is *Sequential Quadratic Programming* (SQP), in order to find the optimum design. The block diagram for the MRB optimization process is shown in Figure 4.4. In order to solve the MRB optimization problem using SA, a design domain was specified as the possible solution space (lower and upper boundaries of this space were defined). Then, the solution of SA initiated a SQP algorithm which searches the optimum using the gradient information and the solutions were updated with the supplied step size and search direction data until the optimum design was found.

4.4 Optimum Design

The optimum dimensional parameters for the magnetic circuit are given in Table 4.2, the corresponding illustration of the optimum design cross-section is shown in Figure 4.5.

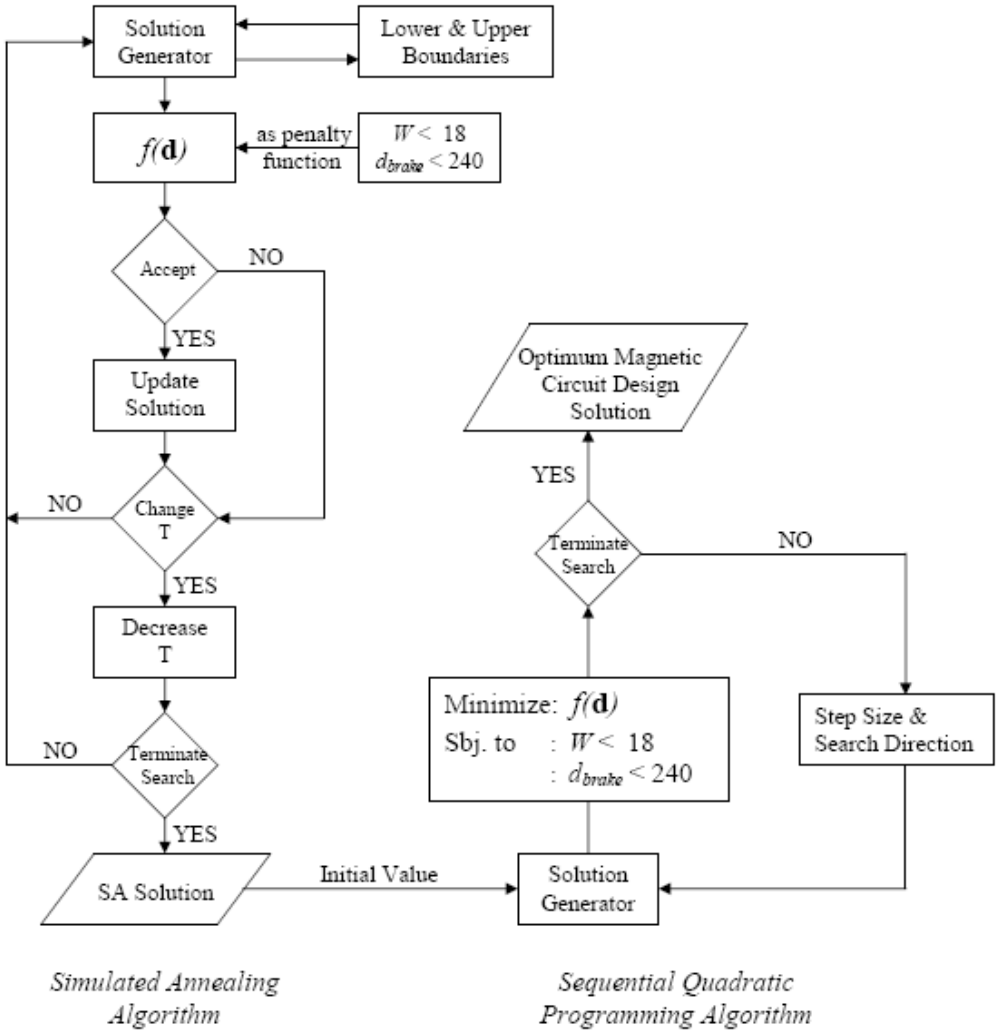

Figure 4.4: MRB optimization process

Table 4.2: Optimum design parameters

Parameter	**Optimum Value (mm)**	**LB - UB (mm)**
$\mathtt{d}_1$	17.11	20 - 80
$\mathtt{d}_2$	18.05	5 - 15
$\mathtt{d}_3$	1.03	2 - 4
$\mathtt{d}_4$	47.34	10 - 80
$\mathtt{d}_5$	5.08	5 - 10
$\mathtt{d}_6$	14.57	4 - 15
$\mathtt{d}_7$	2.07	2 - 20
$\mathtt{d}_8$	10.00	10 - 30
$\mathtt{d}_9$	10.34	5 - 20
$\mathtt{d}_{10}$	3.08	3 - 10
$\mathtt{d}_{11}$	0.91	0.91 - 3.79
$\mathtt{d}_{12}$	2.04	1 - 4

LB: Lower Boundary and UB: Upper Boundary

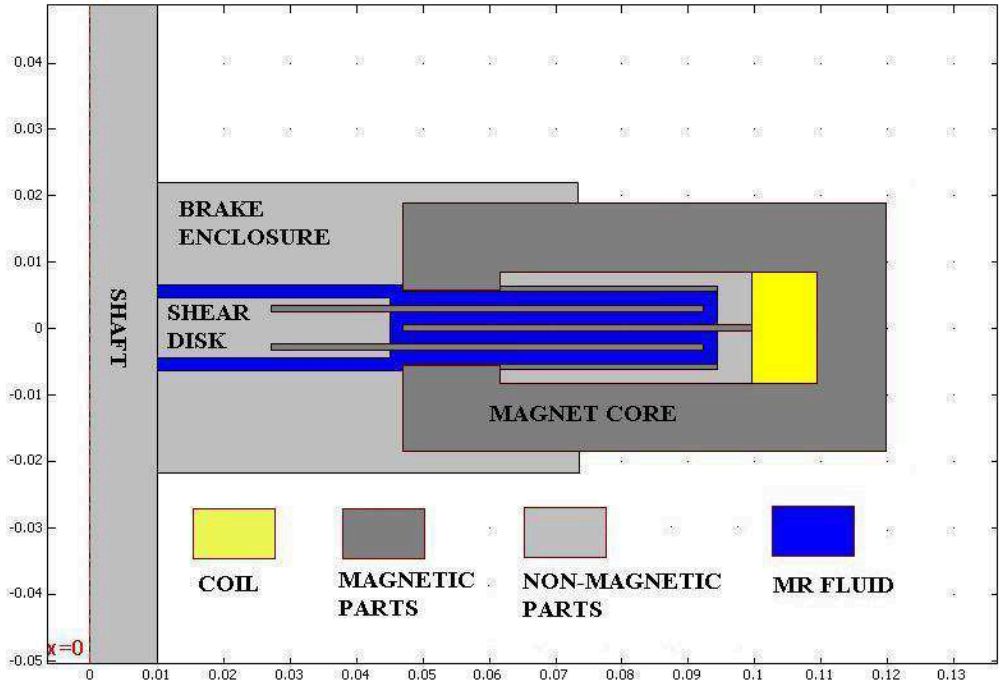

Figure 4.5: Optimum MRB design

In addition, using FEA, magnetic field intensity and magnetic flux density distribution within the MRB were plotted. Figure 4.6 shows the corresponding distributions of field intensity and flux density.

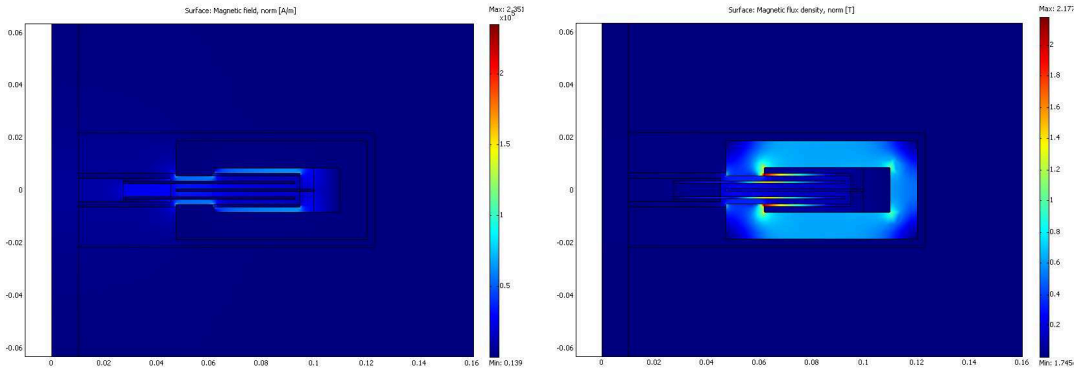

Figure 4.6: i) Magnetic field intensity distribution and ii) Magnetic flux density within optimum MRB design

By using the data plotted in Figure 4.6 and using the analytical model of the MRB (see Bingham Plastic Model, Eq. (2.9)), shear stress distribution generated only due to the magnetic field application within the MRB was illustrated in Figure 4.7. One can easily notice the similarity between the magnetic field intensity and the shear stress distribution plots. Since, the shear stress generated on MR fluid is approximated with a linear function (see Eq. (2.12)), both plots are quite similar in terms of the distribution.

Then, using Eq. (2.14), the braking torque generation was calculated at various current application. The relationship between the applied current and the simulated braking torque generation is shown in Figure 4.8. Since the results do not include the viscous term, the relationship starts from the origin ($T_\mu = 0$ @ 0 A). According to the simulation results, the relationship is almost linear and at 1.8 A, the magnetic

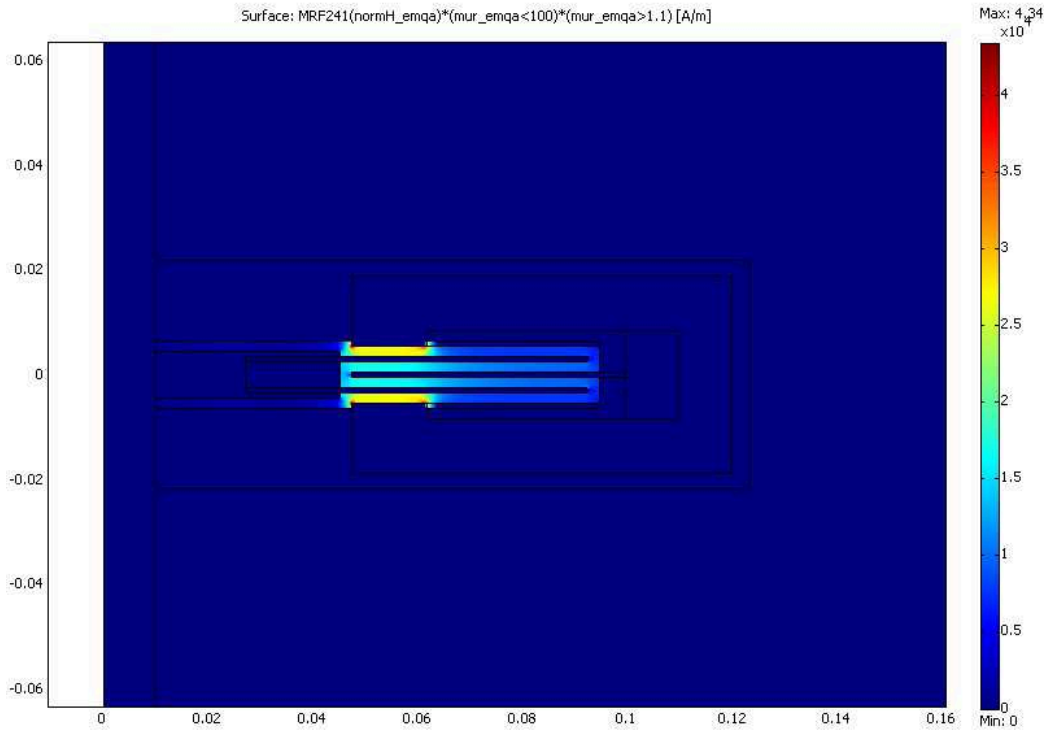

Figure 4.7: Shear stress distribution within optimum MRB

braking torque generated is around 23 Nm.

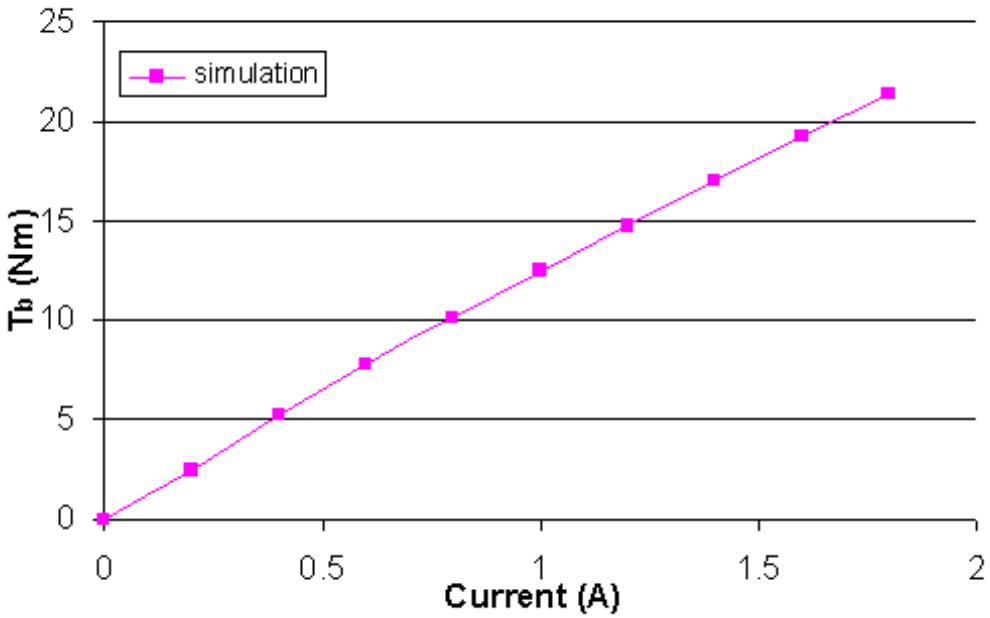

Figure 4.8: Braking torque generation simulation results

Chapter 5

Experimentation

In this chapter, the proposed MRB was prototyped for experimenting its braking performance. The optimum design found in the previous section was used and a prototype was manufactured. This prototype was then mounted onto an experimental test-bed, which included a torque source and a torque sensor to measure the torque generation. The braking torque generated by the MRB prototype was measured at various current density applications to the coil and the results are shown in this chapter.

5.1 Experimental Setup

In order to set up an experiment to measure the braking torque capacity of the proposed design, the optimum MRB design was manufactured and it was mounted to a test-bed. Here, in this section, the overview of the experimental setup is divided into two subsections: i) MRB prototype and ii) MRB test-bed, which contains the sensors and actuators used to test the braking performance of the MRB prototype.

5.1.1 MRB Prototype

After an optimum design was found in the previous chapter by solving the defined optimization problem for the MRB, a 3-D CAD model was generated using Pro/E (see Figure 5.1 (L)). The MRB was slightly modified for ease of manufacturing and additional details such as bearings, seals and the surface finishes were defined. As mentioned in Sec. 3.4, standard Viton O-rings were used for the static and dynamic sealing purposes. In addition, angular ball bearings, 7004 LLB (double sealed and non-contact type), were used. Corresponding seal and bearing locations are shown in Figure 5.1 (R).

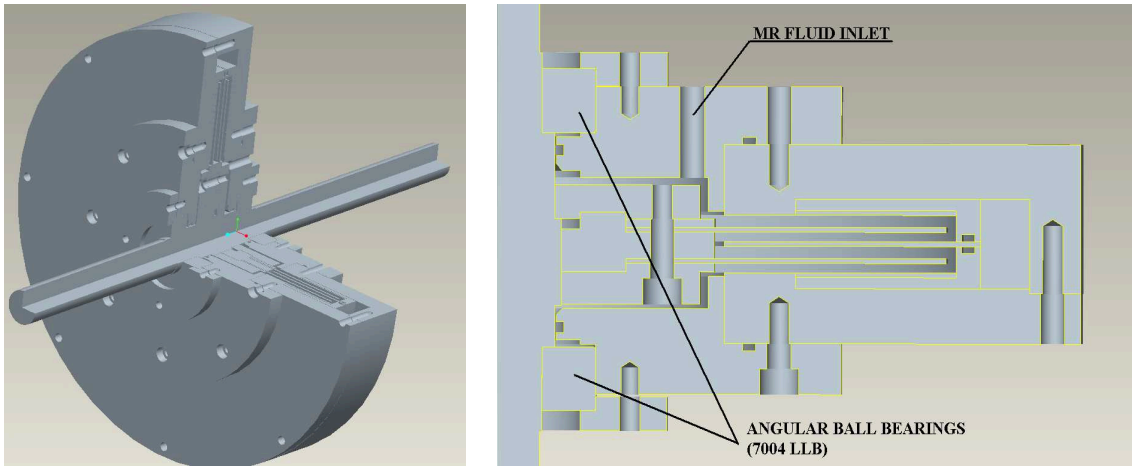

Figure 5.1: MRB CAD model (L) and cross-section of the MRB CAD model with bearings, screw holes and seal beds (R)

Also in Figure 5.1 (R), the location of the screw holes and the MR fluid inlet are shown. In the MRB prototype, 38 screws of various sizes (stainless steel screws were used to assemble the parts that are not parts of the magnetic circuit) were used, and also for the MR fluid inlet, 3 NPT holes were drilled, in order to fill the MRB properly without introducing an air gap.

Then, the MRB prototype components were manufactured according to the 3-D CAD model generated using Pro/E. Then, the parts were assembled and the prototype that is ready for testing is shown in Figure 5.2 (L). The most challenging part of the assembly was the coil, which has to be placed within the MRB static casing that forms the electromagnet i.e. core. The coil has to be one piece for easy installation, thus, a custom bobbin was machined to wind the coil and then the coil wound around the bobbin was installed onto the MRB. In Figure 5.2 (R), the coil and bobbin assembly is shown, which is installed in the MRB's electromagnetic core. Another hole was drilled onto the electromagnetic core for the terminals of the coil (see Figure 5.2 (L)). In addition, in order to measure the temperature of the MR fluid within the MRB, a K-type thermocouple was bonded onto one of the NPT taps, using a high temperature resistant and highly conductive epoxy, OMEGA OB-200.

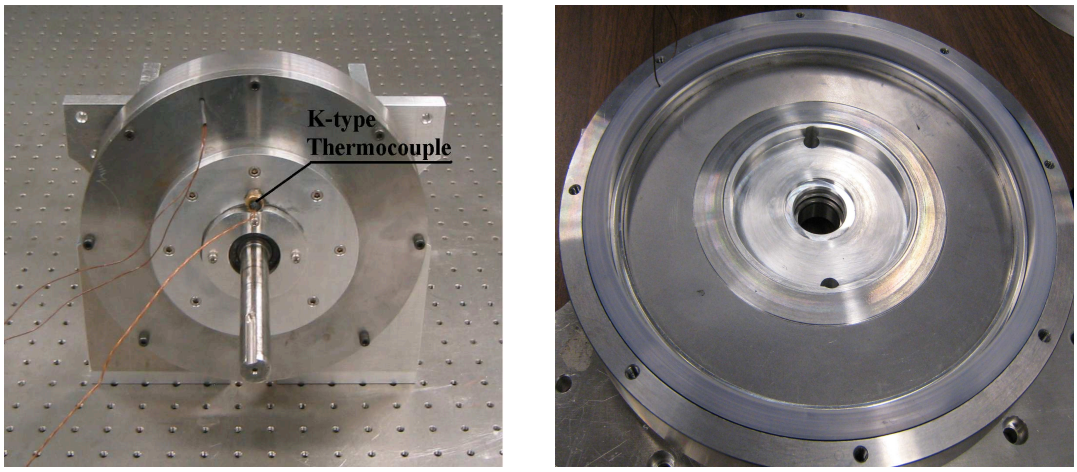

Figure 5.2: MRB prototype (L) and coil assembly (R)

The specifications of the MRB prototype is given in Table 5.1.

Table 5.1: MRB prototype specifications

Weight	11.8 kg
Diameter	239.9 mm
Number of Disks	2
Amount of MR Fluid used	205 cm^3
Coil Wire Size	AWG 21
Number of Turns	236 $\pm$ 2 turns
Max. Current Applied	1.8 A
Max. Current Density Applied	2.54e6 A/m^2
Seals Used	Viton O-rings and Loctite 5900® Flange Sealant
Magnetic Materials Used	Steel 1018
Non-Magnetic Materials Used	Al T-6061 and SS 304
Max. Braking Torque	23 Nm @ 1.8 A

5.1.2 MRB Test-Bed

The MRB prototype was then installed into the experimental setup shown in Figure 5.3. A servo motor from CMC Inc. with a continuous torque of 45.4 lb.in and with rotational speed of 5445 rpm was used to generate the continuous torque. Since the torque generation capacity of the servo motor is relatively low, an ALPHA 0755-MC1-7 gear reducer (7:1) was used. The servo motor was connected to a Futek torque sensor (TRS605) which is a shaft-to-shaft rotary torque sensor with a torque measuring capacity up to 1000 Nm. The other end of the torque sensor was connected to the MRB prototype. An Inertia Dynamics magnetic clutch was installed between the torque sensor and the servo motor in order to release the load on the servo motor generated by the brake. In order to connect the various components, flexible couplings were used. In addition, an OMEGA SMCJ-K, analog amplifier, was used to amplify the output of the K-type thermocouple that was installed to measure the temperature of the MR fluid.

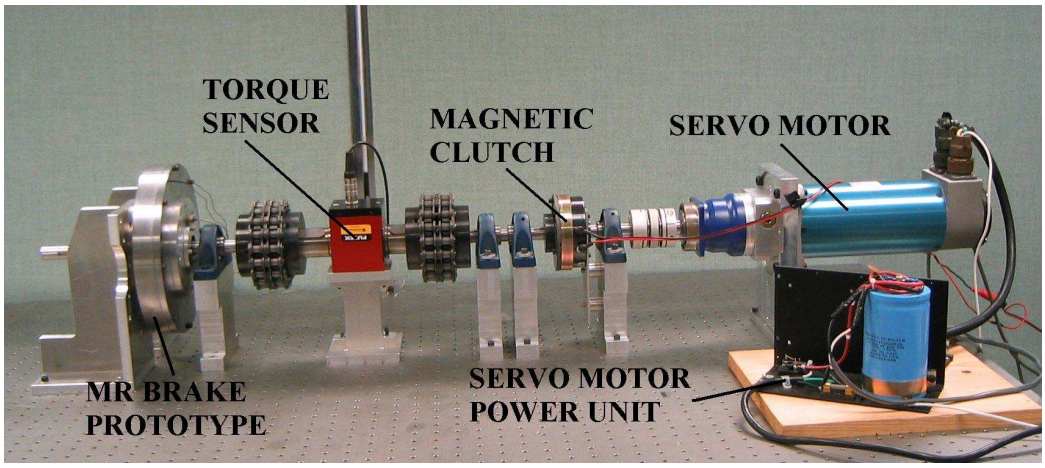

Figure 5.3: Picture of experimental setup

The servo motor was controlled with a PID controller and the rotational speed of

the brake was verified using the encoder embedded in the torque sensor. All input and output signals were connected to a dSPACE control board (DS1104). The control signal from the dSPACE board to the servo was amplified using an Advanced Motion Control Brushless PWM servo amplifier. In addition, a low-pass filter circuit was implemented into the setup in order to reduce the high frequency noise in the torque sensor readings.

During the experiments, the rotational speed was kept constant at various values and current was applied to the coil using an Agilent Technologies high current power supply (N5766A). Whenever the brake was actuated, since the system was at steady-state, the relative torque measured between the shafts on each side of the torque sensor was recorded as the braking torque generated by the brake prototype. After the braking torque data was obtained, the magnetic clutch was turned on in order to release the torque load on the servo motor.

5.2 Validation of the MRB prototype

After the experimental test-bed was physically set up, some sample tests were carried out in order to identify any problems with the data acquisition and signal processing. There were some issues that appeared during these tests, which had to be fixed before the actual data could be collected for the MRB prototype. Then, the MRB was tested and the corresponding results were recorded.

5.2.1 Experimental Problems

During the initial experimentation of the MRB prototype, a number of problems arose. The main problem was the electrical noise interference in the torque sensor

and the thermocouple signals, caused by a ground loop within the electrical circuitry. Most of the noise interference was removed by improving the circuitry and by shielding the system properly. The remaining high frequency noise was removed by using a physical low pass filter, a simple RC circuit, and a nonlinear software filter, which was a Butterworth 6th order filter, designed using Matlab-Simulink Filter Design Toolbox.

Another issue was the leakage of the MR fluid, which was mentioned in Sec. 3.4. Due to the high contamination of the fluid and the loss of flexibility due to the on/off cycle of the MR fluid by applied magnetic field in the vicinity of the seals, the seals had to be properly installed. In the first trial, due to low surface finish quality of the sealing surfaces, leakage occurred. Experiment was repeated after the surface finishes were improved.

In addition to these, a minor problem was the heating of the prototype and also the servo motor. Between two consecutive readings, the temperature of the fluid and the MRB was increased due to applied current and shear friction generation in the MRB. After a set of data was taken, the brake was cooled down to room temperature by using external fans. In addition, since brake generates a torque load against the servo motor, the motor was also heating up. Therefore, between experiments, the servo motor and the MRB prototype were cooled down which prolonged the time duration of the experiments.

5.2.2 Experimental Procedure and Results

First we measured the no-field torque generated by the viscosity of the MR fluid (plus the mechanical friction torque). In Figure 5.4, the torques generated due to viscosity of the fluid at various rotational speeds are shown. The relation between the viscous

torque and speed is linear, as described by Eq. (2.15).

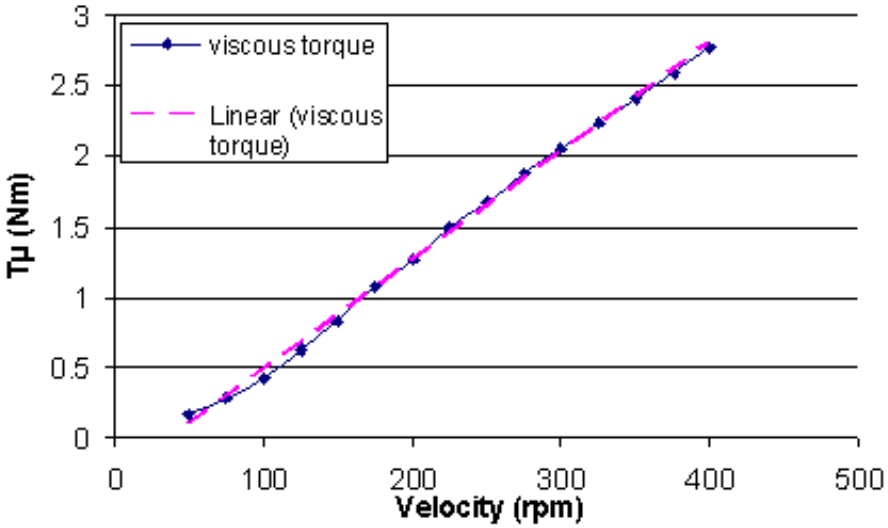

Figure 5.4: Viscous torque versus velocity

After the viscous torque was calculated, current was applied to the electromagnet coil and corresponding change in the torque readings were recorded. Corresponding torque readings at various currents applied are shown in Table 5.2. Figure 5.5 shows the total braking torques (T_b) generated with respect to the increasing speeds. The difference between the three torque curves is directly due to the varying viscous torques (Figure 5.4) at different speeds.

The plots shown in Figure 5.5 contain the viscous effects and the frictional effects. In order to compare the experimental results with the simulation results, the viscous and the friction effects have to be subtracted from the experimental data. The resulting plots between the torque (T_H) generated due to the applied magnetic field and the current applied is shown in Figure 5.6. Three plots are almost identical, which shows that this quantity is not speed dependent, as described by Eq. (2.14).

Table 5.2: Torque generated under various magnetic field intensities

		Torque Generated(Nm) (total)			Torque Generated(Nm) (magnetic term)		
Current Values (A)	Current Density (A/m^2)	100rpm	200rpm	300rpm	100rpm	200rpm	300rpm
0	0	0.426	1.269	2.051	0	0	0
0.2	281677.7	1.329	2.212	3.055	0.903	0.943	1.003
0.4	563355.4	3.316	3.858	4.500	2.890	2.589	2.448
0.6	845033.1	3.898	4.781	5.624	3.472	3.512	3.572
0.8	1126711	6.286	6.848	7.491	5.860	5.579	5.439
1	1408389	8.755	9.478	9.899	8.329	8.209	7.847
1.2	1690066	11.404	12.147	12.468	10.97	10.878	10.416
1.4	1971744	14.575	15.217	15.739	14.149	13.948	13.687
1.6	2253422	17.947	18.394	18.990	17.521	17.125	16.938
1.8	2535099	21.699	22.663	22.944	21.273	21.394	20.892

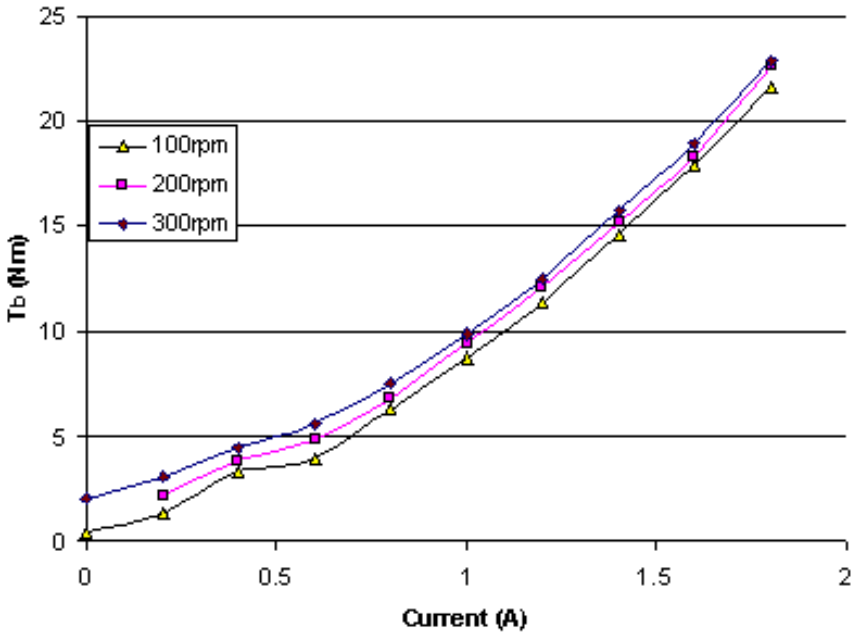

Figure 5.5: Torque (T_b) versus current applied

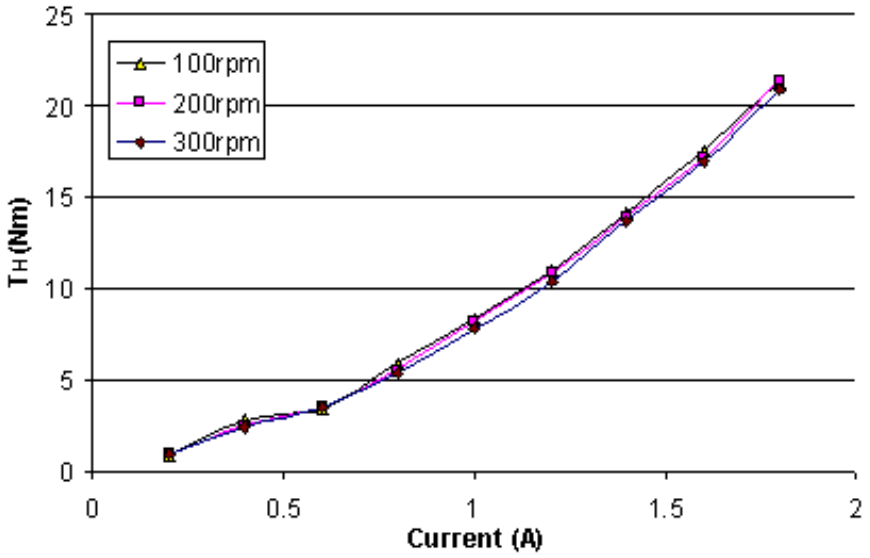

Figure 5.6: Torque (T_h) generated due to magnetic field (without viscous and friction torques)

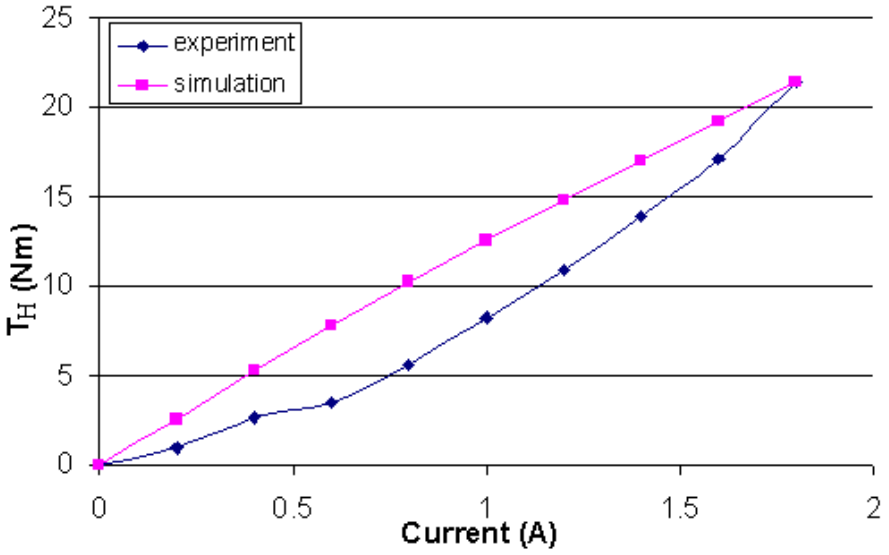

Figure 5.7: Comparison between experimental and simulation results @ 200 rpm

Finally, the simulation and the experimental results are compared in Figure 5.7. While the initial (at 0 A) and final (at 1.8 A) values match, there is deviation in the middle values (104% difference at 0.2 A and 12% difference at 1.6 A). The main reason behind this deviation is probably due to the lack of accurate information on the material properties that were used in the simulations. Another minor factor is the heating in the experimental brake which was not modeled in the FEM. Since temperature rise has an effect on both the magnetic properties and the viscosity of the fluid, either the heating of the brake has to be avoided during the experiment or the FEM has to account for temperature effects.

5.3 Discussion

Note that in order to stop a vehicle (e.g. a 1000 kg passenger vehicle) with an deceleration of 6 m/s^2 (which is the typical requirement for measuring braking performance of a fully loaded passenger vehicle with burnished brakes), each brake has to generate over 500 Nm (see Sec. 2.1.1). The prototyped MRB can generate only 5% of this braking torque. In order to further increase the braking torque a number of improvements can be made:

1. In Figure 5.8, the simulated improvement in the braking torque with additional disks is shown for the same design configuration proposed in this work. However, still, only 20% of the required torque can be generated with an MRB with 7 disks.

2. Another way of increasing the braking torque generation is to change the basic magnetic circuit configuration. In Figure 5.9(L), an MRB with a completely different magnetic circuit configuration is shown without considering the sealing

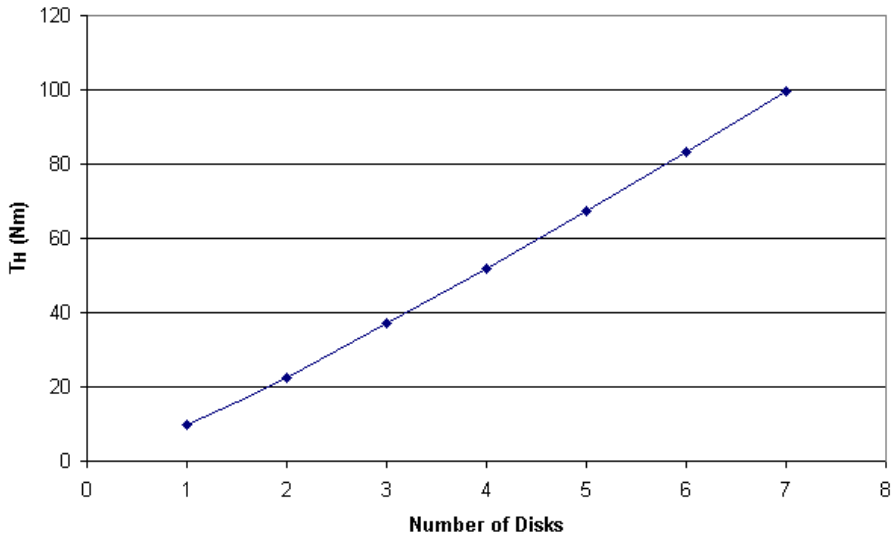

Figure 5.8: Simulation plot of braking torque (T_H) generated with respect to the number of disks (N) (@ 1.8 A)

problem that was discussed in Chapter 3. The magnetic braking torque generation for this configuration at various applied currents is shown in Figure 5.9(R). In this case, 10% of the required braking torque can be generated with only one disk.

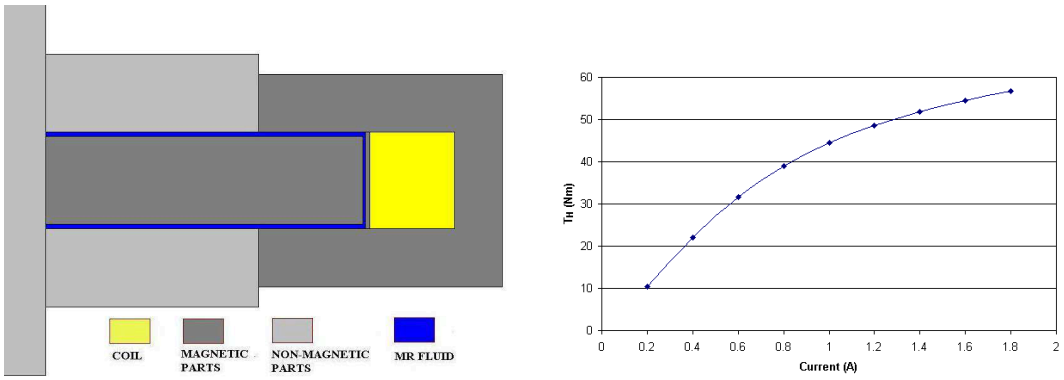

Figure 5.9: An MRB with different magnetic circuit configuration (L) and corresponding simulation plot of braking torque (T_H) vs. applied currents (R)

3. The braking torque capacity can also be increased by relaxing the size and the weight constraints defined in Eqs. (4.7) and (4.8). Note from Table 5.1 that the weight of the prototyped MRB is still lighter than that of the overall CHB system.

With a combination of these improvements, there is a potential to further increase the braking torque capacity of an MRB for the automotive application.

Chapter 6

Conclusion and Future Works

6.1 Conclusion

In this work, a magnetorheological brake (MRB) is introduced as a possible substitute for the conventional hydraulic brake (CHB). Since MRB is an electromechanical device, it has several advantages over CHB, such as the reduced actuation delay, ease of software control implementation and lower system weight. In this work, the design process was started with an analytical model of the proposed MRB. Then, the MRB was designed in detail with a focus on magnetic circuit optimization and material selection. After the candidate MRB design was selected, in order to conduct further optimization analysis, a 2-D finite element model (FEM) of the MRB was created, which simulates the steady-state magnetic flux flow within the MRB domain. This was carried out using COMSOL Electromagnetic Module, which solves for the magnetic field intensity distribution within the FEM of the MRB. The FEM was then used to optimize the magnetic circuit in order to maximize the braking torque and minimize the weight of the MRB. The MRB optimization problem was solved using an integrated optimization code that included simulated annealing and sequential

quadratic algorithms. A 3-D CAD model of the optimum MRB design was then generated and an MRB prototype of the optimum design was manufactured.

The MRB braking performance was tested using an experimental setup that consisted of a torque sensor and a servo motor. The experimental results showed that the braking torque is increased with applied current, reaching more than 20 Nm at 1.8 A, verifying our theoretical predictions. There were discrepancies with respect to the simulation results due to inaccurate material property modeling in the simulations. Thus, in our future work (see Sec 6.2 for more detail), the simulation model will be improved by including the temperature effects and more accurate description of the material properties. In addition, this work showed that the proposed MRB configuration cannot supply enough braking torque to stop a vehicle. Therefore, an improved MRB will be designed with an increased number of disks and a modified magnetic circuit configuration.

6.2 Future Works

The very first thing that has to be done is to improve the correlation between the simulation and the experimental results. The simulation results can be improved to match the experimental data by using a more detailed model of the material properties and by including the temperature effects in the simulation.

As was mentioned previously in Chapter 1, the main objective was to design an EMB which can be used as a substitute for CHB. However, the braking torque generation capacity of the MRB proposed in this work is not high enough for a typical passenger vehicle. Therefore, the braking capacity of the MRB must be improved by relaxing the constraints defined for the MRB optimization problem, i.e. by increasing the number of disks attached and by changing the magnetic circuit configuration (see

Sec. 5.3). This improved MRB then has to be prototyped and tested.

One of the major concerns with the actual implementation of an MRB into a car is the high temperature effect on the MR fluid. In practice, the proposed MRB would likely require a physical (e.g. active or passive) cooling system to alleviate the heating problem in the MR fluid and thus improving the braking performance. Since, the brake actuator transforms kinetic energy into heat, all kinetic energy of the car will be converted into heat in the MRB. As mentioned previously in the material selection section (Sec. 3.3) of this thesis, the magnetic properties are highly dependent on the temperature of the MR fluid (the viscosity varies with temperature). Hence, heat transfer analysis has to be included in future studies.

After the modified MRB is tested, a closed-loop controller has to be designed in order to remove the residual flux generated due to the hysteresis characteristics of the magnetic materials employed in the MRB. This controller will be then combined with other controllers such as an antilock braking controller that avoids slipping of the tires during braking. Then, the MRB and the controllers will be tested on a dynamometer to simulate real road conditions. As the final step, the MRB will be mounted on for a vehicle and tested for on-road performances.

Bibliography

[1] Automotive Systems Division of Continental AG, *Continental Electronic Brake Systems*, Auburn Hills, MI, 2007.

[2] Delphi Co., *Delphi Brake Modules - Electric Caliper*, Troy, MI, 2005.

[3] J. Song, "Performance Evaluation of a Hybrid Electric Brake System with a Sliding Mode Controller", *Mechatronics*, **15**, p339-358, 2005.

[4] E. Simeu and D. Georges, "Modeling and Control of an Eddy Current Brake", *Control Eng. Practice*, **4(1)**, p19-26, 1996.

[5] K. H. Park and K. Lee, *Contactless Eddy Current Brake for Cars*, US Patent 6,286,637 B1, United States Patent Office, Sep. 2001.

[6] K. Lee and K. H. Park, "Optimal Robust Control of a Contactless Brake System Using an Eddy Current", *Mechatronics*, **4**, p615-631, 1999.

[7] K. Lee and Kyi H. Park, "Modeling Eddy Currents With Boundary Conditions by Using Coulomb's Law and the Method of Images", *IEEE Transactions on Magnetics*, **38(2)**, p1333-1340, March 2002.

[8] R.W. Phillips, *Engineering applications of fluids with a variable yield stress*, Ph.D. Thesis, University of California, Berkeley, CA,1969.

[9] S. Genc and P.P. Phule, "Rheological properties of magnetorheological fluids", *Smart Materials and Structures*, **11**, p140-146, 2002.

[10] J. Rabinow , "The magnetic fluid clutch", *AIEE Transactions*, **67**, p1308-1315, 1948.

[11] J. Rabinow. *Magnetic fluid torque and force transmitting device*, US Patent 2,575,360, United States Patent Office, November 20, 1951.

[12] Lord Corporation, *Magnetorheological (MR) Solutions*, Cary, NC, 2007. Available: http://www.lord.com

[13] J. H. Yoo and N. M. Wereley, "Design of a high-efficiency magnetorheological valve", *J. Intel. Mat. Syst. And Structures*, **13(10)**, p679-685, October 2002.

[14] R. Gilbert and M. Jackson. "Magnetic ride control", *GM Tech Link*, **4(1)**, p1-2, January 2002.

[15] J. D. Carlson, "Controlling vibration with magnetorheological fluid damping", *Sensors*, **19(2)**, February 2002.

[16] S.J. Dyke, B.F. Spencer Jr., M.K.Sain and J.D. Carlson, "Modeling and control of magnetorheological dampers for seismic response reduction", *Smart Materials and Structures*, **5**, p565-575, 1996.

[17] L. M. Jansen and S. J. Dyke, "Semi-active control strategies for MR dampers: A comparative study", *ASCE Journal of Engineering Mechanics*, **126(8)**, p795-803, August 2000.

[18] Z. D. Xu, Y. P. Shen and Y. Q Guo, "Semi-active control of structures incorporated with magnetorheological dampers using neural networks", *Smart Materials and Structures*, **12**, p80-87, 2003.

[19] B.M. Kavlicoglu, F. Gordaninejad, C.A. Evrensel, N. Cobanoglu, Y. Liu, A. Fuchs and G. Korol, "A high-torque magnetorheological fluid clutch", *Proceedings of SPIE Conference on Smart Materials and Structures*, San Diego, CA, USA, March 2002.

[20] S. Gopalswamy, S. M. Linzell and G. L. Jones, *Magnetorheological fluid clutch with minimized reluctance*, US Patent 5,845,752, United States Patent Office, December 8 1998.

[21] S. v.L. Henkel, "MR knee is a step up", *Sensors*, **18(1)**, January 2001.

[22] H. Herr, "Prosthetic and orthotic limbs" *Journal of Rehabilitation Research and Development*, **39(3)**, p11-12, May-June 2002.

[23] B. Liu, W. H. Li, P. B. Kosasih and X. Z. Zhang, "Development of an MR-brake-based haptic device", *Smart Materials and Structures*, **15**, p1960-1966, 2006.

[24] G.A. Flores and J. Liu, "In-vitro blockage of a simulated vascular system using magnetorheological fluids as a cancer therapy", *European Cells and Materials*, **3(2)**, p9-11, 2002.

[25] G. Paula, "Exercise equipment puts on magnetorheological brakes", *Mechanical Engineering*, ASME, New York, NY, May 1997.

[26] G.M. Webb, *Exercise apparatus and associated method including rheological fluid brake*, US Patent 5,810,696, United States Patent Office, September 22, 1998.

[27] J.D. Carlson, D.M. Catanzarite and K.A. St. Clair. "Commercial magnetorheological fluid devices", *Proc. 5th Int. Conf. on ER Fluids, MR Fluids and Assoc. Tech.*, p20-28, Singapore, 1996.

[28] G.R. Eddens, "Magnetic particle clutches and brakes: A premier", *Power Transmission Design*, **20(3)**, p58-61, March 1978.

[29] G. R. Eddens, *Magnetic particle brake*, US Patent 3.962.595, United States Patent Office, June 1976.

[30] G. R. Eddens, *Magnetic particle devices*, US Patent 4.350.913, United States Patent Office, Sep. 21, 1982.

[31] J.D. Carlson, D.F. LeRoy, J.C. Holzheimer, D.R. Prindle and R.H. Marjoram, *Controllable brake*, US Patent 5.842.547, United States Patent Office, Dec. 1, 1998.

[32] J.D. Carlson, *Magnetorheological brake with integrated flywheel*, US Patent 6.186.290 B1, United States Patent Office, Feb. 13, 2001.

[33] Lord Corporation Material Division, *MR Brake Product Bulletin MRB-2107-3* , Cary, NC, 2003.

[34] E.J. Park, D. Stoikov, L. Falcao da Luz, and A. Suleman, "A performance evaluation of an automotive magnetorheological brake design with a sliding mode controller", *Mechatronics*, **16**, p405-416, 2006.

[35] W. Zhou, C.M. Chew and G.S. Hong, "Development of a compact double disk magnetorheological fluid brake", *Robotica*, p1-8, note: Published online by Cambridge University Press, Feb. 12, 2007.

[36] J. An and D.S. Kwon, "Modeling of a magnetorheological actuator including magnetic hysteresis", *J. Intel. Mat. Syst. And Structures*, **14(9)**, p541-550, 2003.

[37] E.J. Park, L. Falco da Luz, and A. Suleman, "Multidisciplinary design optimization of an automotive magnetorheological brake" in print *Computers and Structures*, (available online).

[38] L. Falcao Da Luz, *Design of a magnetorheological brake system*, M.A.Sc. Thesis, Department of Mechanical Engineering, University of Victoria, BC, CANADA, 2004.

[39] T. Gillespie, *Fundamentals of Vehicle Dynamics*, SAE, Warrendale, PA, 1992.

[40] D. Cole, *Elementary Vehicle Dynamics*, Course Notes in the Mechanical Engineering, The University of Michigan, Ann Arbor, MI, 1972.

[41] C. Lee, K. Hedrick, and K. Yi, "Real-Time Slip-Based Estimation of Maximum Tire-Road Friction Coefficient", *IEEE/ASME Transactions on Mechatronics*, **9(2)**, June 2004.

[42] A. B. Will, S. Hui and S. Zak, "Sliding Mode Wheel Slip Controller for an Antilock Braking System", *Int. J. of Vehicle Design*, **19(4)**, p523-539, 1998.

[43] W. Kordonsky, "Elements and devices based on magnetorheological effect", *J. Intel. Mat. Syst. And Structures*, **4(1)**, p65-69, 1993.

[44] K.D. Weiss, J.D. Carlson and D.A. Nixon, "Viscoelastic properties of magneto- and electro-rheological fluids", *J. Intel. Mat. Syst. And Structures*, **5(11)**, p772-775, 1994.

[45] R. Stanway, J.L. Sprosten and N.G. Stevens, "Nonlinear identification of an electrorheological vibration damper", *Proceedings of IFAC Symposium on Identification and System Parameter Estimation*, p195-200, 1985.

[46] R.M. Bozorth, *Ferromagnetism*, D. Van Nostrand Company, 1st edition, Princeton, New Jersey, 1951.

[47] M.L. Hodgdon, "Application of a theory of ferromagnetic", *IEEE Trans. Mag.*, **24(1)**, p218-221, 1988.

[48] ASTM International, *Annual Book of ASTM Standards, Magnetic Properties*, **4(3)**, 2005.

[49] N. Ida, *Engineering Electromagnetics*, Springer-Verlag, 1st edition, New York, 2000.

[50] P.J.M. van Laarhoven and E.H.L. Aarts, *Simulated Annealing: Theory and Applications*, D.Reidel Publishing Co., Dordrecht, Holland, 1987.

[51] J. Arora, *Introduction to Optimum Design*, Elsevier Academic Press, San Diego, CA, 2nd ed., 2004.

Appendix A

Maxwell Equations

In 1873, the infamous Scottish scientist James Maxwell wrote *Treatise on Electricity and Magnetism*, in which he summarized the relationship between electrical and magnetic fields that was derived by Faraday, Ampere, Gauss, Coulomb and others. His main purpose was to explain Faraday's ideas into a universal mathematical form. His main contribution was to include the displacement current (that results from the change in the electrical flux intensity (or electric displacement) $\mathbf{D}$) in Ampere's Law (see Eq. A.2) [49]. The field equations known as Maxwell's Equations are:

$$\nabla \times \mathbf{E} = -\frac{\partial \mathbf{B}}{\partial t} \tag{A.1}$$

$$\nabla \times \mathbf{H} = \mathbf{J} + \frac{\partial \mathbf{D}}{\partial t} \tag{A.2}$$

$$\nabla \cdot \mathbf{D} = \rho \tag{A.3}$$

$$\nabla \cdot \mathbf{B} = 0 \tag{A.4}$$

where $\mathbf{E}$ is the electric field intensity, $\mathbf{H}$ is the magnetic field intensity, $\mathbf{B}$ is the magnetic flux density, $\mathbf{J}$ is the electric current density and ρ is the charge density.

Eq. (A.1) is known as *Faraday's Law of Induction* which states that any change in the magnetic field results in the flow of charges in a conductive medium. Eq. (A.2) is the *Maxwell-Ampere's Law* which states that electric current flowing through a closed loop results in magnetic field generation. Eqs. (A.3) and (A.4) are known as *Gauss Law*. Eq. (A.3) states that the divergence of electrical flux density is equal to the charge density and Eq. (A.4) states that the divergence of magnetic flux density is always zero for a closed surface defined.

PARTIAL COPYRIGHT LICENSE

Title of Thesis:

Design of a Magnetorheological Brake System Based on Magnetic Circuit Optimization

Author: _____

Kerem Karakoc

_____

Date